Coupled Slow and Fast Charge Dynamics in Cesium Lead Bromide Perovskite

Ali Moeed Tirmzi,[†] Ryan P. Dwyer,[†] Tobias Hanrath,[‡] and John A. Marohn[*,†]

[†]*Department of Chemistry and Chemical Biology, Cornell University, Ithaca, New York 14853*

[‡]*School of Chemical and Bimolecular Engineering, Cornell University, Ithaca, New York 14853*

E-mail: jam99@cornell.edu

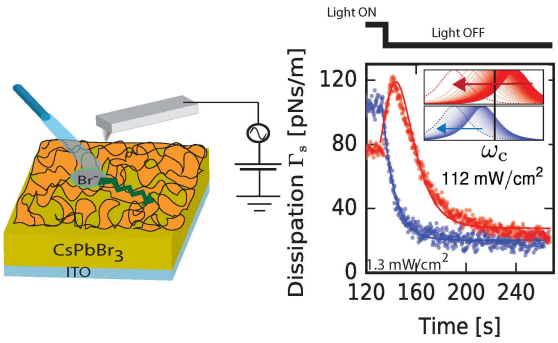

Abstract

Metal halide perovskites show slow (from seconds to minutes) and fast (millisecond to sub microseconds) charge dynamics. We use scanning Kelvin probe microscopy and dissipation microscopy to probe these charge dynamics in a thin film of $CsPbBr_3$. We demonstrate the existence of a light-intensity-dependent τ_{fast} in $CsPbBr_3$ that exhibits a slow, activated, intensity-independent recovery in the dark. The observed τ_{fast}, while

highly light dependent, remained essentially unchanged when the light was turned off, taking $10 \pm 2\,\mathrm{s}$ to relax at room temperature. The data presented here shows direct evidence that the slow and fast charge dynamics ubiquitously seen in lead-halide perovskites have a common origin related to a highly activated charge redistribution.

Lead-halide perovskites have recently emerged as a class of photovoltaic material exhibiting remarkably high power-conversion efficiency while at the same time being inexpensive and simple to synthesize.[1] What makes the lead-halide perovskites such successful photovoltaic materials is a topic of intense interest,[2–6] particularly as highly stable, lead-free replacement materials are sought.[7–11] It has become increasingly clear that these materials change their properties in response to both electric fields and light. Perovskite-type compounds have long been known to undergo ion migration;[12,13] it is therefore not unexpected that these materials exhibit hysteric electrical behavior resulting from electric-field-induced ion motion.[14–16] Applying light, alone or in concert with an electric field, leads to additional and surprising property changes.[16–18] Characterization of lead-halide perovskite devices has revealed large light-induced shifts in current-voltage curves,[14,19–23] impedance spectra and capacitance,[14,24–30] recombination lifetime,[31] photoluminescence lifetime and intensity,[31–33] optical absorption spectra,[34] and Raman spectra.[32]

The mechanisms underlying these light-induced changes is a topic of current debate. Lead-halide perovskites exhibit *slow* charge dynamics on the seconds-to-minutes time scale and *fast* charge dynamics on the milliseconds-to-microseconds timescale. Both slow and fast dynamics are light dependent. The consensus opinion is that slow light-related dynamics involve ion motion. Evidence in support of this hypothesis is provided by electrochemical measurements,[14] scanned probe microscopy,[15] optical microscopy[33] and spectroscopy,[35] mass spectrometry,[33] and X-ray diffraction.[34,36] Fast light-related sample dynamics appear in electrochemical impedance spectra as an intensity-dependent RC time with the R usually attributed to a recombination resistance.[25,26,28,30,37,38] Pockett et al. observed in $MAPbI_{3-x}Cl_x$ that slow and fast charge dynamics depended on light intensity and temperature in the same

way, leading them to conclude that ion motion underlies both light-induced accumulation of interface charges and interfacial charge recombination.[28] van Reenen and coworkers introduced, through modeling studies, the hypothesis that device hysteresis in perovskite solar cells requires *both* ion migration through the bulk *and* subsequent ion-related recombination of charge carriers at the perovskite interface.[21] Understanding both slow and fast dynamics may therefore be crucial to harnessing perovskites in photovoltaic applications.

Here we study a prototypical inorganic lead-halide perovskite, $CsPbBr_3$, prepared as a thin film on an indium tin oxide substrate. We choose $CsPbBr_3$ because it is more robust to light- and temperature-induced degradation than methylammonium lead halide perovskites[39] and it contains a single halide, obviating concerns about light-induced phase segregation. We use scanning Kelvin probe microscopy[40] (SKPM) and dissipation microscopy[41] to make contact-free measurements of (1) the sample's impedance spectrum versus light intensity and (2) the gradual recovery of the sample's fast response time in the dark versus temperature. This data offers clear evidence that the slow and fast charge dynamics ubiquitously seen in lead-halide perovskites have a common origin related to a highly activated charge redistribution.

Figure 1a shows the experimental setup. To describe the following experiments, we found it necessary to develop a new, more comprehensive description of the SKPM measurement that captures the dependence of cantilever frequency and amplitude on the complex sample impedance. This more complete description of the tip-sample interaction allows us to describe the cantilever tip-sample force on the seconds to nanoseconds time scale, even though the sample's response—and correspondingly the charge and electrostatic force—changes dramatically over these time scales. The electrostatic force F on the scanned probe tip depends on sample properties through the tip-sample charge q:

$$F(x,q) = \frac{C'(x)}{2C(x)^2} q(x, V_{\mathrm{ts}})^2, \tag{1}$$

where x is the tip displacement, $C(x)$ the tip capacitance, $C'(x) = dC/dx$, and q depends on displacement x and the applied tip-sample voltage V_{ts}. The time-dependent charge can be well-approximated by

$$q(t) = \Big(C(x(t))\,(V_{\mathrm{ts}}(t) - \phi) \Big) * H(t), \tag{2}$$

where ϕ is the sample surface potential and $*$ denotes convolution in the time domain. In the frequency domain, the transfer function H between applied tip-sample voltage V_{ts} and the tip voltage drop $V_{\mathrm{t}} = q/C$ is

$$\hat{H}(\omega) = \frac{\hat{V}_{\mathrm{t}}(\omega)}{\hat{V}_{\mathrm{ts}}(\omega)} = \frac{1/(j\omega C_{\mathrm{tip}})}{Z(\omega) + 1/(j\omega C_{\mathrm{tip}})}, \tag{3}$$

where Z is the sample impedance and $C_{\mathrm{tip}} = C(0)$. To describe dynamics on the ms to µs timescale, we model the sample as a parallel resistor R_{s} and capacitor C_{s}. The sample impedance is given by $Z = (R_{\mathrm{s}}^{-1} + j\omega C_{\mathrm{s}})^{-1}$ (Figure 1b). The resulting transfer function H is a lag compensator with time constant τ_{fast} and gain parameter g given by

$$\tau_{\mathrm{fast}} = R_{\mathrm{s}}(C_{\mathrm{s}} + C_{\mathrm{tip}}) = R_{\mathrm{s}}C_{\mathrm{tot}} \;\text{ and }\; g = C_{\mathrm{tot}}/C_{\mathrm{s}}. \tag{4}$$

In Figure 1c, we modulate the tip voltage at frequencies ω_{m} much less than the cantilever's resonance frequency ω_{c}. We measure the resulting displacement $x = F/k \propto \hat{q}(\omega_{\mathrm{m}}) \propto \hat{H}(\omega_{\mathrm{m}})$, where k is the cantilever spring constant. Consistent with other measurements,[28] we see evidence for both slow dynamics on the seconds and longer timescale (τ_{slow}) and fast dynamics on the sub-millisecond time scale (τ_{fast}). In subsequent measurements, we focus on the light and time dependence of the τ_{fast} dynamics using the simple, single-time-constant model described above.

Rather than modulating the tip voltage, we can apply a fixed voltage V and modulate the force F by oscillating the cantilever at its resonance frequency ω_{c}. The resulting oscillating

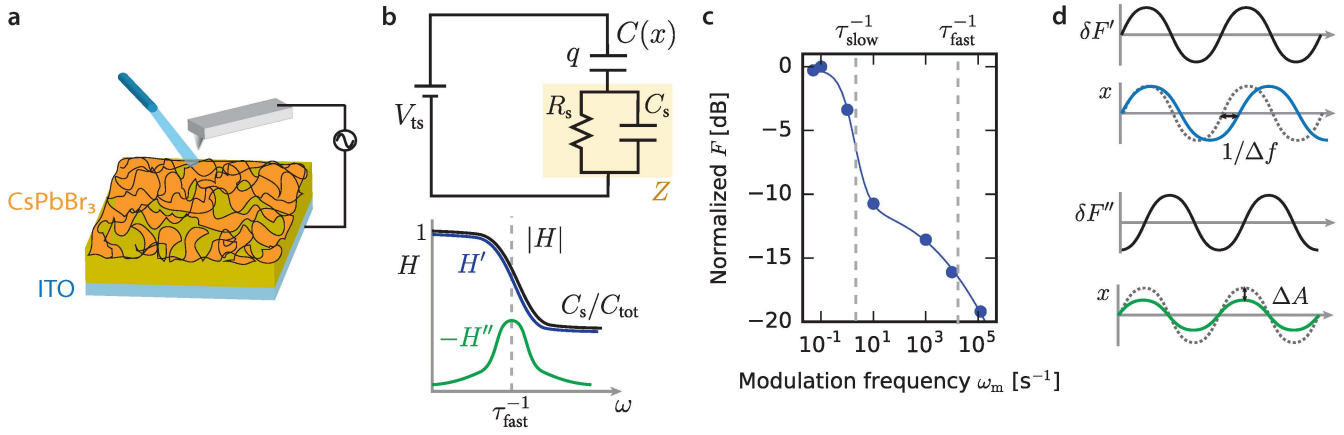

Figure 1: Scanned-probe impedance measurements on a $CsPbBr_3$ perovskite thin film. (a) The experimental setup. Illumination is provided by a 405 nm fiber-coupled laser. (b) The equivalent circuit for the cantilever and sample and the associated response function H (upper, blue: real part, H'; lower, green: imaginary part, H''). (c) Normalized force F vs. modulation frequency. (d) The in-phase and out-of-phase force components lead to frequency and amplitude shifts, respectively.

force is

$$\delta\hat{F} = \frac{1}{2}\Big(C_q'' + \Delta C''\hat{H}(\omega_c)\Big)\,(V-\phi)^2\,\hat{x} \tag{5}$$

where C_q'' is the capacitance second derivative at constant charge, $\Delta C'' = 2(C')^2/C$ and $C'' = C_q'' + \Delta C''$ (see Supporting Information Section S2). The transfer function H evaluated at the cantilever resonance frequency determines the relative phase between F and x. Forces oscillating in phase and out of phase with the cantilever motion affect the cantilever differently. The oscillating force has the form

$$\delta\hat{F} = \underbrace{\delta F'}_{\substack{\text{in-phase,}\\ \text{conservative}}} + \underbrace{j\delta F''}_{\substack{\text{out-of-phase,}\\ \text{dissipative}}}. \tag{6}$$

As shown in Figure 1d, $\delta F'$ shifts the cantilever's frequency by Δf while $\delta F''$ shifts the cantilever's amplitude by ΔA through an additional sample dissipation Γ_s:

$$\Delta f = -\frac{f_c}{2k}\frac{\delta F'}{A} \quad \text{and} \quad \Gamma_s = -\frac{1}{\omega_c}\frac{\delta F''}{A}. \tag{7}$$

For the simple RC model of Figure 1b, the frequency shift and dissipation are

$$\Delta f = -\frac{f_c}{4k}\left(C_q'' + \Delta C'' \frac{1 + g\,\omega_c^2\tau_{fast}^2}{1 + g^2\,\omega_c^2\tau_{fast}^2}\right)\left(V - \phi\right)^2 \tag{8}$$

$$\Gamma_s = \frac{\Delta C''}{\omega_c}\frac{(g-1)\,\omega_c\tau_{fast}}{1 + g^2\,\omega_c^2\tau_{fast}^2}\left(V - \phi\right)^2, \tag{9}$$

where τ_{fast} and g are given by Eq. 4. Both the cantilever frequency shift and the dissipation measure the sample's impedance at the cantilever frequency, $Z(\omega_c)$. Typically the sample impedance at the resonance frequency is assumed to be insignificant: $Z(\omega_c) = 0$ and consequently $H(\omega_c) = 1$ (see Eq. 3). In this approximation, $\delta F' = \frac{1}{2}C''(V-\phi)^2 A$ and $\delta F'' = 0$ so that $\Delta f = -f_c C''(V-\phi)^2/(4k)$ and $\Gamma_s = 0$. Our RC model thus recovers the approximate equations for the sample-induced frequency and dissipation widely used in the SKPM measurement in the limit that $\omega_c\tau_{fast} \to 0$. As we will show, while this approximation may be valid for most organic and inorganic semiconductors, it does not hold in the perovskite sample studied here.

We used a cantilever with resonance frequency $\omega_c \sim 1\,\mu s^{-1}$, so frequency and amplitude shift measurements probed the τ_{fast} dynamics (Figure 1c). We measured cantilever frequency and amplitude versus DC voltage at different light intensities (Figure 2(a, b)). At each light intensity $I_{h\nu}$, we fit the cantilever frequency versus voltage data to

$$f(V) = f_c - \alpha(V - \phi)^2. \tag{10}$$

The maximum of the frequency shift versus voltage parabola corresponds to the surface potential ϕ, while the parabola curvature α is related to the in-phase component of the oscillating electrostatic force $\delta F'$. The amplitude versus voltage curves of Figure 2b measure sample-induced dissipation Γ_s and therefore the out-of-phase component of the oscillating electrostatic force $\delta F''$. The sample-induced dissipation is related to the tip voltage by the equation $\Gamma_s = \gamma_s(V-\phi)^2$ with γ_s a sample-dependent proportionality constant. The observed

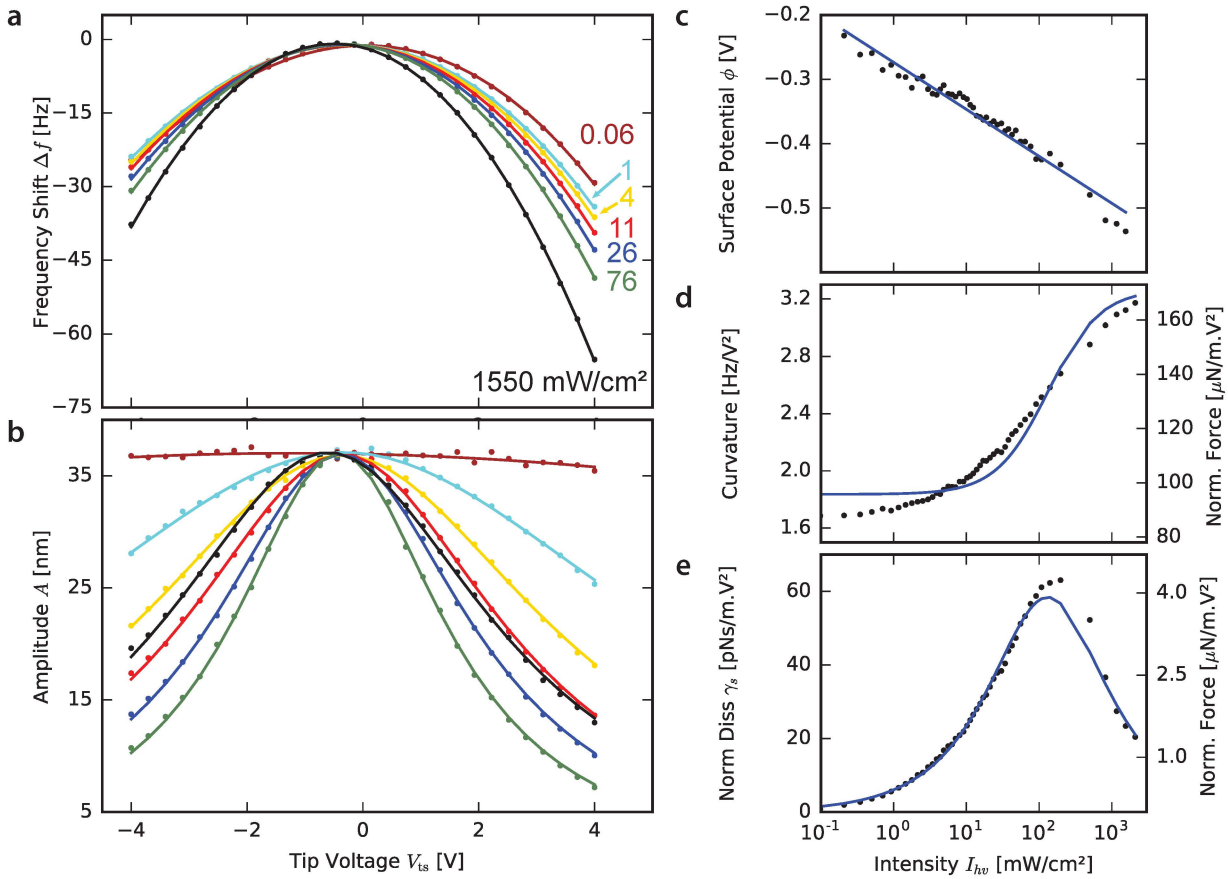

Figure 2: Frequency and amplitude response of cantilever driven in constant-excitation mode at different tip voltages in the presence of constant above-band-gap excitation (405 nm) measured at a tip-sample distance $h = 200\,\text{nm}$. Raw data and best-fit curve for simultaneously acquired (a) frequency shift and (b) amplitude response for seven representative light intensities. The frequency shift and amplitude data from $N = 50$ light intensities was used to calculate, as a function of light intensity, the (c) surface potential, (d) frequency-shift-versus-voltage parabola curvature, and (e) a normalized dissipation constant. Best fit lines in (d) and (e) are modeled using a light-intensity-dependent equivalent circuit representation.

quadratic dependence of dissipation on voltage indicates that the tip charge is not affecting the sample fluctuations responsible for the dissipation.[42] We fit the amplitude-versus-voltage data to extract γ_s (see Experimental Methods).

Figure 2c shows the surface potential increasing with the logarithm of the light intensity at a slope of 72 mV/decade, which is consistent with the expected value of 60 mV/decade ($2.303\,k_B T/e$) for a surface charge density that increases linearly with light intensity.[43] Figure 2d shows an increase in curvature with illumination, similar to the photocapaci-

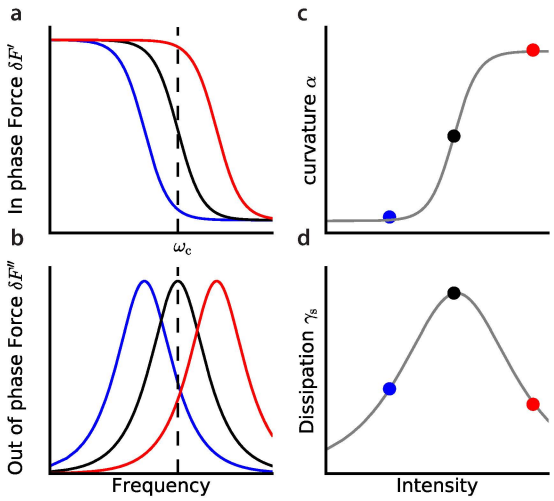

Figure 3: A light-dependent τ_{fast} explains both frequency and amplitude data. (a) In-phase and (b) out-of-phase force for various values of τ_{fast} according to Eq. 3, Eq. 5, and the transfer function of Fig. 3b. Left, blue curve: slow τ_{fast}, low $I_{h\nu}$; middle, black curve: intermediate τ_{fast}, intermediate $I_{h\nu}$; and right, red curve: short τ_{fast}, high $I_{h\nu}$. Measurements probe the force at the cantilever frequency, $\delta\hat{F}(\omega_c)$; the cantilever frequency is indicated as a dotted vertical line in (a,b). The predicted intensity dependence of the (c) frequency-vs-voltage curvature α and (d) dissipation γ_s agrees with the Figure 2(d,e) data.

tance effect seen by Ginger et al. and others in organic semiconductor films.[44–48] Surprisingly, Figure 2e shows that the sample-induced dissipation peaks at a certain light intensity. While the exact intensity where the maximum dissipation occurred was affected by light exposure history and local sample inhomogeneities, the qualitative appearance of the plots in Figure 2(c-e) was similar across the film over a period of weeks. We rule out photodegradation related dissipation because the curvature and dissipation data were reproducible after resting in the dark.

While a photocapacitance effect could explain the curvature data (Figure 2d), it cannot explain the dissipation data (Figure 2e). Instead, we propose that both the curvature and dissipation data can be understood in a unified way by postulating that the sample's τ_{fast} decreases with increasing light intensity:

$$\tau_{\text{fast}}(I_{h\nu}) = \tau_0 (I_{h\nu}/I_0)^{-n}. \tag{11}$$

with I_0 a reference intensity, τ_0 a reference charge-response time, and n a unitless exponent. The effect of a decreasing τ_{fast} on curvature α and dissipation γ_s is explained qualitatively in Figure 3. In combination with the impedance model described above, the Eq. 11 postulate allows us to quantitatively fit the measured curvature and dissipation (Fig. 2d and Fig. 2e, respectively). With $\tau_0 = \omega_c^{-1} = 2.5\,\mu s$, we find a best-fit exponent $n = 0.6$ and maximum-dissipation intensity $I_0 = 100\,\text{mW}\,\text{cm}^{-2}$. Over the range of light intensities shown in Figure 2, the best-fit time constant τ_{fast} decreases from 190 µs at low intensity to 390 ns at high intensity. This simple model with only one light-intensity-dependent time constant explains the main features of both dissipation and curvature changes and estimates the time scale for τ_{fast}. The changes in τ_{fast} could be due to photo-conductivity. There is evidence that these perovskite materials have low conductivity in the dark which increases considerably on light exposure.[49] With increasing light intensity, the conductivity of the sample increases, decreasing τ_{fast} and moving the roll-off of the sample's response to higher frequencies (Fig. 3a). When the sample time constant τ_{fast} equals the inverse of the cantilever frequency $\omega_c^{-1} = 2.5\,\mu s$, sample-induced dissipation reaches a maximum (Fig. 2e, Fig. 3(b,d)). As the light intensity is further increased, the out-of-phase charge motion begins to decrease.

To provide further evidence for τ_{fast} decreasing with increasing light intensity, we used a variant of broadband local dielectric spectroscopy[50] (BLDS) to probe the sample's response across a wide range of frequencies (Figure 4). We applied a tip-sample voltage $V_{ts} = \phi - V_m + V_m \cos(\omega_m t)$ so that the sample charge was always positive (e.g., $V_{ts}(t)$ always less than ϕ). We measured $\Delta f_{\text{BLDS}}(\omega_m) = \Delta f_{\text{DC}}(V_m = 2.83\,\text{V}) - \Delta f_{\text{DC}}(V_m = 0)$, the difference in DC cantilever frequency shift Δf_{DC} with the modulation on and off. This experiment chiefly measures the *magnitude* of the sample's response at the modulation frequency $|\hat{H}(\omega_m)|$ (see Supporting Information Section S2B, Equation S26). To clearly show that that the sample's time constant changes with light intensity, we plot a normalized frequency shift $\Delta f_{\text{norm}} = \Delta f_{\text{BLDS}}(\omega_m)/\Delta f_{\text{BLDS}}(2\pi \times 0.1\,\text{Hz})$. The Δf_{norm} vs. modulation frequency data shows a characteristic cut-off frequency τ_{fast}^{-1} arising from the sample's complex impedance.

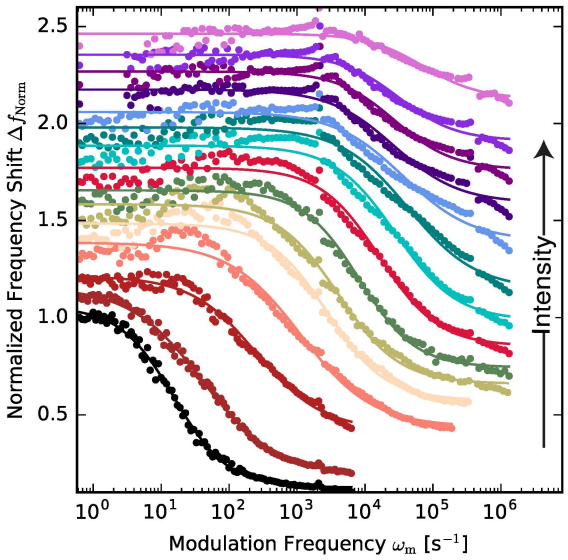

Figure 4: Normalized frequency shift vs. modulation frequency for increasing light intensities (offset vertically by 0.1 for clarity). The surface potential ϕ was measured before the start of each measurement at each new light intensity. The cantilever frequency was averaged for an integer number of cycles of the AC modulation to suppress frequency shift components at harmonics of the modulation frequency. $I_{h\nu}$ from bottom to top: 0, 0.064, 0.512, 1.28, 3.2, 4.8, 12.8, 22, 33, 49, 83, 112, 176, 685, and 2095 $\mathrm{mW/cm^2}$.

The Figure 4 data shows that with increasing light intensity, the cut-off frequency moves to higher frequencies, corresponding to a shorter τ_{fast}. At low light intensities, the normalized frequency shift approaches zero for $\omega_{\mathrm{m}} \gg \tau_{\mathrm{fast}}^{-1}$. This high-frequency behavior implies that the sample capacitance C_{s} was small compared to the tip capacitance C_{tip} (see Figure 1b, Equation S4). Over the range of intensities studied, the sample's fast time constant $\tau_{\mathrm{fast}} \approx R_{\mathrm{s}}C_{\mathrm{tip}}$ (Equation 4), and the large decrease in τ_{fast} is therefore primarily due to a large light-induced decrease in R_{s} in our experiment. At higher light intensities, the normalized frequency shift does not approach zero for $\omega_{\mathrm{m}} \gg \tau_{\mathrm{fast}}^{-1}$, which would be consistent with C_{s} increasing with light intensity. This increase in C_{s}, while clearly observable, would have only a small effect on the time constant τ_{fast}.

Our findings so far show that the R_{s} underlying $CsPbBr_3$'s fast charge dynamics is strongly affected by illumination, even in a sample with no top contact present. To test the hypothesis that the dependence of τ_{fast} on light involves ion or vacancy motion, we

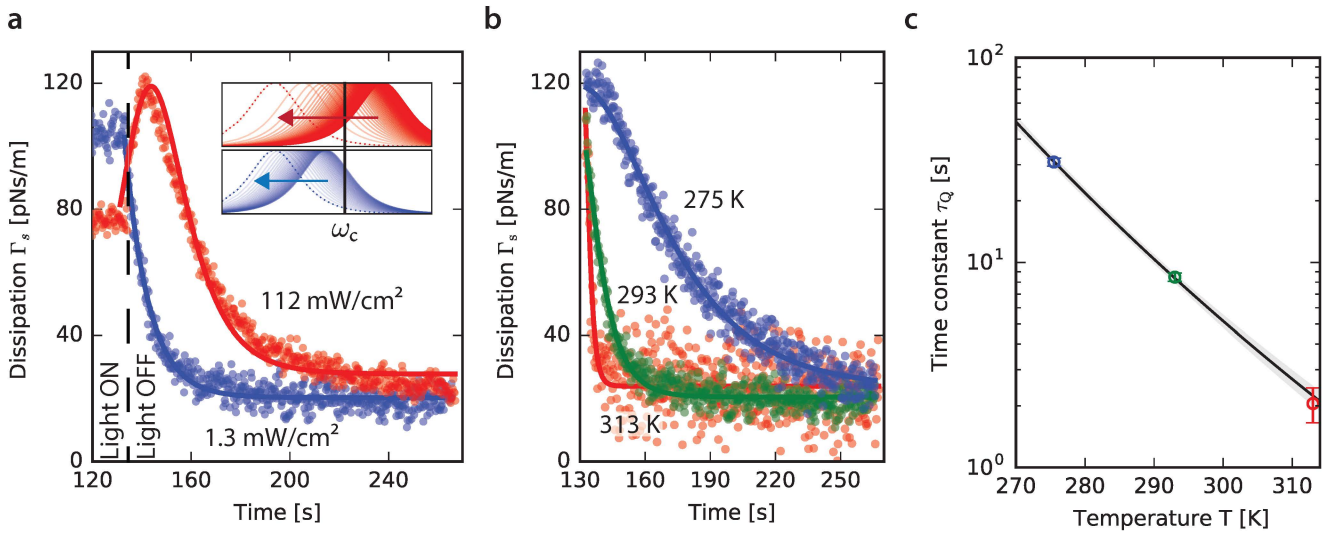

Figure 5: Sample-induced dissipation in the dark after a period of continuous illumination ($V_{ts} = 4\,V$, $h = 200\,nm$, and $\phi = -250 \pm 50\,mV$). The light was switched off after 133 s of pre-soaking illumination. (a) The upper (red) data used an initial intensity $I_{h\nu} = 112\,mW/cm^2$, greater than the maximum-dissipation intensity. The lower (blue) data used $I_{h\nu} = 1.3\,mW/cm^2$, less than the maximum-dissipation intensity. Inset: The out-of-phase cantilever force vs. frequency spectrum evolving in time as τ_{fast} relaxes; the measured dissipation is the value of the spectrum at the cantilever frequency (dotted vertical line). The peak dissipation seen in the upper (red) curve occurs when the peak of the out-of-phase cantilever force spectrum coincides with the cantilever frequency. (b) Raw data and best fit for dissipation at three temperatures ($I_{h\nu} = 1.12\,mW\,cm^{-2}$). (c) Time constant for Q recovery vs. temperature with error bars calculated from the fits in (b). The shaded region represents 2 standard deviations for a weighted least squares fit to an exponential model $\tau_Q(T) = A^{-1}\exp(E_a/k_BT)$. The best fit parameters with two standard deviation error bars were $E_a = 0.52 \pm 0.03\,eV$ and $A = 1.4 \pm 1.0 \times 10^8\,s^{-1}$.

used sample-induced dissipation to track changes in τ_{fast} *in real time*. In the experiment of Figure 5, we apply a tip voltage $V_{ts} = 4\,V$ and continuously monitor cantilever dissipation using ring-down measurements. The dissipation Γ was calculated by inferring the cantilever quality factor Q from the measured ring-down time constant and using the cantilever's known spring constant and resonance frequency (Equation **??**).[51,52] This method provides much faster time resolution ($\sim 0.1\,s$) than the amplitude-versus-voltage curve measurement of Figure 2. At $t = 0$, we begin illuminating the sample at an intensity $I_{h\nu}$. The measured cantilever dissipation abruptly increases, reflecting an abrupt decrease in the sample resistance R_s caused by the illumination (time constant $< 0.1\,s$, see Figure S7). After

133 s, we turn off the light and the dissipation returns to its initial dark value (Figure 5). If the intensity $I_{h\nu}$ was greater than the maximum-dissipation intensity, we observed an initial increase in dissipation, *in the dark,* before dissipation began to decrease (red points). Sample-induced dissipation initially increased despite the fact that photocarriers were no longer being generated. Such a dissipation peak was not observed when $I_{h\nu}$ was less than the dissipation-maximum intensity (blue points). As shown in the Figure 5 inset, these observations are consistent with the Fig. 3 schematic and τ_{fast} increasing from sub-µs to ms when the light is switched off. As it relaxes towards its light-off value, τ_{fast} passes through a point where it is equal to the inverse of the cantilever frequency, $\omega_c^{-1} = 2.5\,\mu\text{s}$, and dissipation reaches a maximum (Figure 3). The relaxation rate is relatively insensitive to the applied DC tip voltage (Figure S3). Surprisingly, the time scale of the τ_{fast} recovery in the dark—from seconds to minutes—is orders of magnitude slower than the initial decrease in τ_{fast} when the light is switched on. The time scale of the τ_{fast} recovery in the dark points towards the slow dynamics governing the evolution of the fast dynamics.

To investigate the process responsible for the slow changes in dissipation, we measured the temperature dependence of this Q recovery time constant τ_Q (Fig. 5(b, c)). In these experiments we used $I_{h\nu}$ less than the maximum-dissipation intensity. Over a 40 °C range, τ_Q changes from 2 s to 31 s. This large change clearly indicates that a highly activated process is responsible for changes in τ_Q. We deduce an activation energy of $0.52 \pm 0.03\,\text{eV}$ (95 % confidence interval). Figure 5 is the central finding of our manuscript.

In the above mathematical treatment, the dissipation data of Figures 2e and 5 arose from the out-of-phase response of the driven sample charges. We can equivalently think about dissipation as arising from sample fluctuations. As a consequence of the fluctuation-dissipation theorem of statistical mechanics, the driven response probed in the Figure 4 experiment must be accompanied by sample voltage and electric field fluctuations. In this view, dissipation arises from cantilever charge coupling to fluctuations having spectral density at frequency ω_c.[42,51,53–55] The usefulness of this point of view is that different microscopic

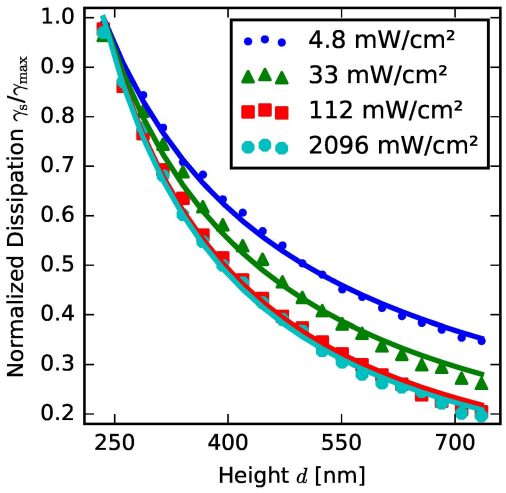

Figure 6: Height dependence of dissipation at four different light intensities. At each height, the cantilever frequency and amplitude measurement of Figure 2(a,b) was performed. From low to high light intensity, $\gamma_{max} = 10$, 36, 62, and 35 $\mathrm{pN\,s\,m^{-1}\,V^{-2}}$.

models of charge fluctuations predict a Γ_s with a distinct height dependence. Scanned probe microscope studies of dissipation versus height can therefore potentially give insight into the microscopic origin of the fast charge dynamics in perovskites and related samples.

In Figure 6 we plot the normalized dissipation vs. tip height measured at four light intensities. The dependence of γ_s on height h approximately follows a power law, $\gamma_s \propto h^{-n}$, with an exponent n evolving from 0.9 at low intensity to 1.3 at high intensity. This is a remarkably weak dependence on height that is not well modeled by prior microscopic descriptions of dissipation arising from dielectric fluctuations,[42,51] diffusing charges,[54,55] thermal position fluctuations of confined charges, or charge blinking,[46] either in bulk or at the sample surface. The height dependence becomes steeper (larger n) at higher intensity, qualitatively consistent with the movement of fluctuating charges, ions, or defects towards the upper sample surface as the light intensity is increased.

The experiments reported here confirm the ability of scanning probe microscopy to collect local dielectric spectra over six decades of frequency.[50,56] We introduced a modified form of the broadband local dielectric spectroscopy experiment and a revised mathematical treatment of scanning Kelvin probe microscopy (SKPM) that depends explicitly on the sample

impedance. The revised treatment revealed that the usually-employed description of the SKPM experiment makes the implicit assumption that tip charge adjusts adiabatically as the cantilever oscillates. This assumption breaks down in the $CsPbBr_3$ sample at low illumination intensities. Observing a transition from the non-adiabatic to adiabatic tip-charge limit in a single experiment is unprecedented in scanning probe microscopy.

Our microscopic impedance spectroscopy measurement represents the most detailed examination of light-dependent fast dynamics in $CsPbBr_3$ to date. The measured surface potential shows the textbook dependence on light intensity that one would expect for a band-transport semiconductor in which charge density depends linearly on intensity.[43,57] The light intensity dependence of the sample's τ_{fast} dynamics was measured in two ways. In the Figure 2 experiment the tip oscillation acted as a small voltage modulation, while in the Figure 4 experiment we applied a large voltage modulation. Both measurement gave similar results for τ_{fast}. The τ_{fast} measured here for $CsPbBr_3$ is the same order of magnitude and shows a similar dependence on light intensity as the fast charge-response time reported in impedance measurements of $MAPbI_{3-x}Cl_x$ devices,[28] suggesting that a light-dependent fast charge-response time may be a general feature of lead halide perovskites. This suggestion is consistent with recent reports that the optoelectronic properties of $CsPbBr_3$ are very similar to those of the hybrid perovskites.[4]

The central finding of this manuscript is the existence of a light-intensity-dependent τ_{fast} in $CsPbBr_3$ that exhibits a slow, activated, intensity-independent recovery in the dark. The observed τ_{fast}, while highly light dependent, remained essentially unchanged when the light was turned off, taking $10 \pm 2\,\text{s}$ to relax at room temperature. Moreover, the τ_{fast} recovery time (τ_Q, Figure 5) showed insignificant changes over two decades of soaking light intensity. The recovery time τ_Q had a magnitude, intensity dependence, and activation energy ($E_a = 0.52 \pm 0.03\,\text{eV}$) consistent with the slow charge dynamics (timescale τ_{slow}) previously attributed to ion or defect motion in lead-halide perovskites.[14,15,33–36] In single-crystal $CsPbBr_3$, Mizusaki and coworkers measured a $0.25\,\text{eV}$ activation energy for halide

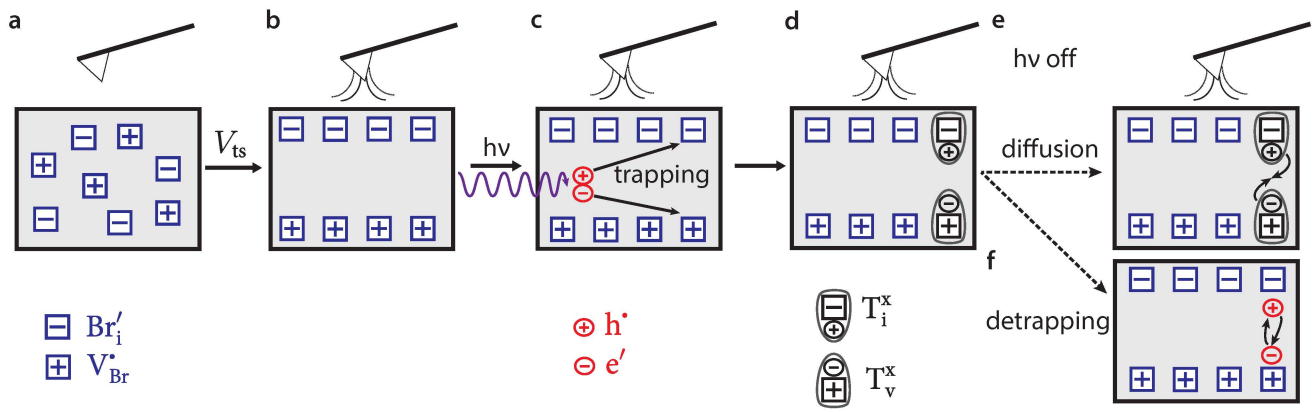

Figure 7: Proposed mechanisms for slow activated recovery of τ_{fast}. (a) Random distribution of ionic charge in the material in the dark. (b) In response to an applied tip voltage, ionic charges redistribute on the timescale τ_{slow}. (c) When the light is switched on, electrons and holes are generated. (d) Electrons and holes trap at the oppositely charged ionic center, forming neutral species. When the light is turned off, either (e) the neutral specie diffuses until electron and hole are close enough to recombine, or (f) electrons and/or holes detrap and recombine.

transport in the intrinsic region and 0.72 eV in the extrinsic region.[12] Our E_a is consistent with these values, although we emphasize that our measurements were performed on a thin film and not on a single crystal.

Let us now use what is known about $CsPbBr_3$ and related materials to attempt to develop a microscopic picture of charge motion consistent with the data presented here. Comparing to prior work, it is reasonable to conclude that τ_{slow} arises from ion motion. The challenge is to explain the dependence of τ_{fast} on light intensity, time, and temperature. The time constant τ_{fast} probes R_s, the resistance associated with charge rearranging in the sample in response to the oscillating tip voltage It is helpful to think in terms of conductivity, $\sigma_s \propto 1/R_s$. Ideally, our microscopic picture should explain (1) the observation that $\sigma_s \propto I_{h\nu}$ over a four-decade range of light intensity; (2) the persistence of σ_s immediately after the light is turned off; and (3) the slow, activated return of the sample to a low-conductivity state.

Consider the nature, concentration, and distribution of charged species present in the experiment of Figure 5. We first apply a voltage to the cantilever, then apply light to

the sample. The positive tip voltage will attract negative ions upward and repel positive ions downward (Fig. 7(a,b)). The concentration of ionic defects in the sample is expected to be significant; the concentration of positive bromide vacancies, for example, can be $\rho_{\text{ion}} \geq 10^{18}\,\text{cm}^{-3}$ in lead-halide perovskites.[18,23,28,58] The applied light will primarily generate free charge carriers (Fig. 7c). Taking $I_{h\nu} = 100\,\text{mW}\,\text{cm}^{-2}$ and assuming that all the incident light is absorbed in a 300 nm thick layer, we estimate a charge generation rate of approximately $G \sim 10^{22}\,\text{cm}^{-3}\,\text{s}^{-1}$; given the reported monomolecular recombination coefficient $k_1 \sim 10^7\,\text{s}^{-1}$, the maximum density of photo-generated electronic free carriers would be ca. $\rho_{\text{e}} \sim 10^{15}\,\text{cm}^{-3}$.[4] The concentration of photoinduced carriers is thus orders of magnitude smaller than the ion concentration.[14]

The conductivity σ_{s} could be due to either mobile ions or electronic charge carriers. If σ_{s} is due to ionic conductivity then observation (1) requires that either the ionic-carrier mobility or ionic-carrier concentration must increase linearly with light intensity. Neither of these hypotheses seems likely. On the other hand, if σ_{s} is due to electronic conductivity, (1) is just the expected linear dependence of free electronic carrier density on light intensity. However, we know of no precedent for photoinduced free carriers persisting for many seconds; the hypothesis that σ_{s} is due to free electronic carriers is therefore seemingly inconsistent with (2). We are led to the rather surprising conclusion that if σ_{s} is due to electronic charge, then nearly all of the electronic charge must be trapped. Yang and coworkers reached a similar conclusion in their conductivity studies of hybrid organic-inorganic lead-halide perovskites.[14] Even if nearly all of the electronic charge is trapped, however, the 10 s trap-clearing time seems anomalously long.

It is difficult to see how electronic or ionic charge alone explains both (1) and (2). Therefore, we next consider specific states that couple electronic and ionic charge. Many of the ionic defects expected to be present in perovskites are thought to act as shallow donors and acceptors;[59,60] in Fig. 7(c,d) we therefore show electronic free carriers trapping at the ionic

defects. Bromide interstitials and vacancies are plausible defects; in Kröger–Vink notation,

$$\mathrm{V}_{\mathrm{Br}}^{\bullet} + \mathrm{e}' \rightleftharpoons \underbrace{(\mathrm{V}_{\mathrm{Br}}^{\bullet} \cdots \mathrm{e}')}_{\mathrm{T}_{\mathrm{v}}^{\mathrm{x}}} \tag{12}$$

$$\mathrm{Br}_{\mathrm{i}}' + \mathrm{h}^{\bullet} \rightleftharpoons \underbrace{(\mathrm{Br}_{\mathrm{i}}' \cdots \mathrm{h}^{\bullet})}_{\mathrm{T}_{\mathrm{i}}^{\mathrm{x}}}. \tag{13}$$

where $\mathrm{T}_{\mathrm{v}}^{\mathrm{x}}$ and $\mathrm{T}_{\mathrm{i}}^{\mathrm{x}}$ represent the vacancy and interstitial sites occupied by a trapped electron and hole, respectively. What would this coupled ionic-electronic trap state add to our picture? A conductivity σ_{s} proportional to $[T_{\mathrm{v}}^{x}]$ or $[T_{\mathrm{i}}^{x}]$ could be consistent with both (1) and (2). If σ_{s} is due to ionic conductivity, then the ionic conductivity could be dominated by ions at the $\mathrm{T}_{\mathrm{v}}^{\mathrm{x}}$ and $\mathrm{T}_{\mathrm{i}}^{\mathrm{x}}$ sites. If σ_{s} is due to electronic conductivity, Equations 12 and 13 offer a potential mechanism for the charge trapping invoked to explain (2). If trapped at shallow defects, then electronic carriers at the $\mathrm{T}_{\mathrm{v}}^{\mathrm{x}}$ and $\mathrm{T}_{\mathrm{i}}^{\mathrm{x}}$ sites must dominate the conductivity. Alternatively, ionic defects can act as deep traps,[59,60] with equilibria nearly identical to those given above. Filling of deep traps with photocarriers would affect the conductivity through changes in the recombination resistance. In either case, the insight is that it is plausible the trap state concentration is (1) linearly dependent on light intensity; and (2) increases quickly when the light is initially turned on and decays slowly in the dark.

The large measured activation energy (3) points to a mechanism of σ_{s} recovery involving ion or defect rearrangements. In Figure 7 we show the neutral trap complexes T^{v} and T^{i} diffusing until the trapped electron and hole get close enough to recombine (Figure 7e). The diffusion constants and therefore E_{a} of the neutral trap complexes would presumably be similar to the diffusion constant for ion motion. Alternatively, the electron and hole detrap from their complexes on the seconds timescale and the resulting free charge carriers quickly recombine (typically $\sim$ 0.1 to 10 µs; Figure 7f). In this scenario, the measured activation energy is the activation energy for trap clearing.

Above we have presented a microscopic picture that includes the species likely to be

present in our $CsPbBr_3$. The known properties of $CsPbBr_3$ do not easily explain our data. Depending on whether σ_s is ionic or electronic, an anomalous dependence of the ionic conductivity on light intensity or an electronic conductivity controlled by the concentration of an extremely long-lived trap state must be proposed. In a similarly difficult to explain measurement, Belisle and co-workers observed a 1 second optical memory effect in photocurrent measurements on methylammonium lead iodide solar cells with asymmetric contacts.[18] Their proposed explanations for this memory effect include large light-induced changes to ionic conductivity, light-induced changes to the contact selectivity, or a high concentration of long-lived charge traps. Here we show that, in a related material without organic cations, τ_{fast} likewise shows a seconds-timescale memory effect. We agree with Belisle and co-workers that our present understanding of the lead-halide perovskites does not explain the memory effect particularly well. The dissipation data of Figure 6 provides one way to independently confirm or refute proposed mechanisms. The use of scanning Kelvin probe microscopy to observe time-dependent and light-dependent local impedance spectra and their accompanying electrical fluctuations opens up many exciting possibilities for understanding light-driven charge, ion, and defect motion in perovskite and other related solid state materials.

Experimental Methods

See Supporting Information for experimental details.

SUPPORTING INFORMATION AVAILABLE

The Supporting Information contains: experimental details regarding the sample and scanned probe microscopy; scanned probe impedance microscopy theory; large voltage modulation experiment details; tip voltage effect on Q recovery; evidence for multiple time constants; large voltage modulation experiment for negative sample charge; fit details for Figure 5; fit details for Figure 2c.

AUTHOR INFORMATION

Corresponding Author

*E-mail: jam99@cornell.edu

Faculty webpage: http://chemistry.cornell.edu/john-marohn

Research group webpage: http://marohn.chem.cornell.edu/

Author Contributions

A.T., R.D., and J.M. designed the experiments. A.T. and T.H. prepared the sample. A.T. and R.D. performed the experiments and analyzed the data. A.T., R.D., and J.M. wrote the paper. All authors discussed the data and revised the manuscript.

Notes

The authors declare no competing financial interest.

Acknowledgement

The authors acknowledge David T. Moore[61] for extended discussions and for sharing data prior to publication. The authors acknowledge the financial support of Cornell University and the U.S. National Science Foundation (Grant DMR-1309540). This work made use of the Cornell Center for Materials Research Shared Facilities which are supported through the NSF MRSEC program (DMR-1120296).

(1) Zhang, W.; Eperon, G. E.; Snaith, H. J. Metal Halide Perovskites for Energy Applications. *Nat. Energy* **2016**, *1*, 16048.

(2) Egger, D. A.; Edri, E.; Cahen, D.; Hodes, G. Perovskite Solar Cells: Do We Know What We Do Not Know? *J. Phys. Chem. Lett.* **2015**, *6*, 279–282.

(3) Zhu, H.; Miyata, K.; Fu, Y.; Wang, J.; Joshi, P. P.; Niesner, D.; Williams, K. W.; Jin, S.; Zhu, X.-Y. Screening in Crystalline Liquids Protects Energetic Carriers in Hybrid Perovskites. *Science* **2016**, *353*, 1409–1413.

(4) Zhu, H.; Trinh, M. T.; Wang, J.; Fu, Y.; Joshi, P. P.; Miyata, K.; Jin, S.; Zhu, X.-Y. Organic Cations Might Not Be Essential to the Remarkable Properties of Band Edge Carriers in Lead Halide Perovskites. *Adv. Mater.* **2017**, *29*, 1603072.

(5) Ono, L. K.; Qi, Y. Surface and Interface Aspects of Organometal Halide Perovskite Materials and Solar Cells. *J. Phys. Chem. Lett.* **2016**, *7*, 4764–4794.

(6) Niesner, D.; Zhu, H.; Miyata, K.; Joshi, P. P.; Evans, T. J. S.; Kudisch, B. J.; Trinh, M. T.; Marks, M.; Zhu, X.-Y. Persistent Energetic Electrons in Methylammonium Lead Iodide Perovskite Thin Films. *J. Am. Chem. Soc.* **2016**, *138*, 15717–15726.

(7) Sun, Y.-Y.; Agiorgousis, M. L.; Zhang, P.; Zhang, S. Chalcogenide Perovskites for Photovoltaics. *Nano Lett.* **2015**, *15*, 581–585.

(8) Hong, F.; Saparov, B.; Meng, W.; Xiao, Z.; Mitzi, D. B.; Yan, Y. Viability of Lead-Free Perovskites With Mixed Chalcogen and Halogen Anions for Photovoltaic Applications. *J. Phys. Chem. C* **2016**, *120*, 6435–6441.

(9) Volonakis, G.; Filip, M. R.; Haghighirad, A. A.; Sakai, N.; Wenger, B.; Snaith, H. J.; Giustino, F. Lead-Free Halide Double Perovskites via Heterovalent Substitution of Noble Metals. *J. Phys. Chem. Lett.* **2016**, *7*, 1254–1259.

(10) Gupta, S.; Bendikov, T.; Hodes, G.; Cahen, D. $CsSnBr_3$, A Lead-Free Halide Perovskite for Long-Term Solar Cell Application: Insights on SnF_2 Addition. *ACS Energy Lett.* **2016**, *1*, 1028–1033.

(11) Savory, C. N.; Walsh, A.; Scanlon, D. O. Can Pb-Free Halide Double Perovskites Support High-Efficiency Solar Cells? *ACS Energy Lett.* **2016**, *1*, 949–955.

(12) Mizusaki, J.; Arai, K.; Fueki, K. Ionic Conduction of the Perovskite-type Halides. *Solid State Ion.* **1983**, *11*, 203–211.

(13) Frost, J. M.; Walsh, A. What Is Moving in Hybrid Halide Perovskite Solar Cells? *Acc. Chem. Res.* **2016**, *49*, 528–535.

(14) Yang, T.-Y.; Gregori, G.; Pellet, N.; Grätzel, M.; Maier, J. The Significance of Ion Conduction in a Hybrid Organic-Inorganic Lead-Iodide-Based Perovskite Photosensitizer.

Angew. Chem. Int. Ed. **2015**, *54*, 7905–7910.

(15) Yuan, Y.; Chae, J.; Shao, Y.; Wang, Q.; Xiao, Z.; Centrone, A.; Huang, J. Photovoltaic Switching Mechanism in Lateral Structure Hybrid Perovskite Solar Cells. *Adv. Energy Mater.* **2015**, *5*, 1500615.

(16) Yuan, Y.; Huang, J. Ion Migration in Organometal Trihalide Perovskite and Its Impact on Photovoltaic Efficiency and Stability. *Acc. Chem. Res.* **2016**, *49*, 286–293.

(17) Gottesman, R.; Zaban, A. Perovskites for Photovoltaics in the Spotlight: Photoinduced Physical Changes and Their Implications. *Acc. Chem. Res.* **2016**, *49*, 320–329.

(18) Belisle, R. A.; Nguyen, W. H.; Bowring, A. R.; Calado, P.; Li, X.; Irvine, S. J. C.; McGehee, M. D.; Barnes, P. R. F.; O'Regan, B. C. Interpretation of Inverted Photocurrent Transients in Organic Lead Halide Perovskite Solar Cells: Proof of the Field Screening by Mobile Ions and Determination of the Space Charge Layer Widths. *Energy Environ. Sci.* **2017**, *10*, 192–204.

(19) Snaith, H. J.; Abate, A.; Ball, J. M.; Eperon, G. E.; Leijtens, T.; Noel, N. K.; Stranks, S. D.; Wang, J. T.-W.; Wojciechowski, K.; Zhang, W. Anomalous Hysteresis in Perovskite Solar Cells. *J. Phys. Chem. Lett.* **2014**, *5*, 1511–1515.

(20) Unger, E. L.; Hoke, E. T.; Bailie, C. D.; Nguyen, W. H.; Bowring, A. R.; Heumüller, T.; Christoforo, M. G.; McGehee, M. D. Hysteresis and Transient Behavior in Current-Voltage Measurements of Hybrid-Perovskite Absorber Solar Cells. *Energy Environ. Sci.* **2014**, *7*, 3690–3698.

(21) van Reenen, S.; Kemerink, M.; Snaith, H. J. Modeling Anomalous Hysteresis in Perovskite Solar Cells. *J. Phys. Chem. Lett.* **2015**, *6*, 3808–3814.

(22) Zhao, C.; Chen, B.; Qiao, X.; Luan, L.; Lu, K.; Hu, B. Revealing Underlying Processes Involved in Light Soaking Effects and Hysteresis Phenomena in Perovskite Solar Cells. *Adv. Energy Mater.* **2015**, *5*, 1500279.

(23) Richardson, G.; O'Kane, S. E. J.; Niemann, R. G.; Peltola, T. A.; Foster, J. M.; Cameron, P. J.; Walker, A. B. Can Slow-moving Ions Explain Hysteresis in the Current–

voltage Curves of Perovskite Solar Cells? *Energy Environ. Sci.* **2016**, *9*, 1476–1485.

(24) Juarez-Perez, E. J.; Sanchez, R. S.; Badia, L.; Garcia-Belmonte, G.; Kang, Y. S.; Mora-Sero, I.; Bisquert, J. Photoinduced Giant Dielectric Constant in Lead Halide Perovskite Solar Cells. *J. Phys. Chem. Lett.* **2014**, *5*, 2390–2394.

(25) Pockett, A.; Eperon, G. E.; Peltola, T.; Snaith, H. J.; Walker, A.; Peter, L. M.; Cameron, P. J. Characterization of Planar Lead Halide Perovskite Solar Cells by Impedance Spectroscopy, Open-Circuit Photovoltage Decay, and Intensity-Modulated Photovoltage/Photocurrent Spectroscopy. *J. Phys. Chem. C* **2015**, *119*, 3456–3465.

(26) Pascoe, A. R.; Duffy, N. W.; Scully, A. D.; Huang, F.; Cheng, Y.-B. Insights Into Planar $CH_3NH_3PbI_3$ Perovskite Solar Cells Using Impedance Spectroscopy. *J. Phys. Chem. C* **2015**, *119*, 4444–4453.

(27) Almond, D. P.; Bowen, C. R. An Explanation of the Photoinduced Giant Dielectric Constant of Lead Halide Perovskite Solar Cells. *J. Phys. Chem. Lett.* **2015**, *6*, 1736–1740.

(28) Pockett, A.; Eperon, G.; Sakai, N.; Snaith, H.; Peter, L. M. P.; Cameron, P. J. Microseconds, milliseconds and seconds: deconvoluting the dynamic behaviour of planar perovskite solar cells. *Phys. Chem. Chem. Phys.* **2017**, DOI: 10.1039/c6cp08424a.

(29) Zarazua, I.; Bisquert, J.; Garcia-Belmonte, G. Light-Induced Space-Charge Accumulation Zone as Photovoltaic Mechanism in Perovskite Solar Cells. *J. Phys. Chem. Lett.* **2016**, *7*, 525–528.

(30) Zarazua, I.; Han, G.; Boix, P. P.; Mhaisalkar, S.; Fabregat-Santiago, F.; Mora-Seró, I.; Bisquert, J.; Garcia-Belmonte, G. Surface Recombination and Collection Efficiency in Perovskite Solar Cells From Impedance Analysis. *J. Phys. Chem. Lett.* **2016**, 5105–5113.

(31) Stranks, S. D.; Burlakov, V. M.; Leijtens, T.; Ball, J. M.; Goriely, A.; Snaith, H. J. Recombination Kinetics in Organic-Inorganic Perovskites: Excitons, Free Charge, and Subgap States. *Phys. Rev. Applied* **2014**, *2*, 034007.

(32) Gottesman, R.; Gouda, L.; Kalanoor, B. S.; Haltzi, E.; Tirosh, S.; Rosh-Hodesh, E.; Tischler, Y.; Zaban, A.; Quarti, C.; Mosconi, E.; De Angelis, F. Photoinduced Reversible Structural Transformations in Free-Standing $CH_3NH_3PbI_3$Perovskite Films. *J. Phys. Chem. Lett.* **2015**, *6*, 2332–2338.

(33) deQuilettes, D. W.; Zhang, W.; Burlakov, V. M.; Graham, D. J.; Leijtens, T.; Osherov, A.; Bulovic, V.; Snaith, H. J.; Ginger, D. S.; Stranks, S. D. Photo-induced Halide Redistribution in Organic–inorganic Perovskite Films. *Nat. Commun.* **2016**, *7*, 11683.

(34) Hoke, E. T.; Slotcavage, D. J.; Dohner, E. R.; Bowring, A. R.; Karunadasa, H. I.; McGehee, M. D. Reversible Photo-induced Trap Formation in Mixed-halide Hybrid Perovskites for Photovoltaics. *Chem. Sci.* **2015**, *6*, 613–617.

(35) Yoon, S. J.; Draguta, S.; Manser, J. S.; Sharia, O.; Schneider, W. F.; Kuno, M.; Kamat, P. V. Tracking Iodide and Bromide Ion Segregation in Mixed Halide Lead Perovskites During Photoirradiation. *ACS Energy Lett.* **2016**, *1*, 290–296.

(36) Beal, R. E.; Slotcavage, D. J.; Leijtens, T.; Bowring, A. R.; Belisle, R. A.; Nguyen, W. H.; Burkhard, G. F.; Hoke, E. T.; McGehee, M. D. Cesium Lead Halide Perovskites With Improved Stability for Tandem Solar Cells. *J. Phys. Chem. Lett.* **2016**, *7*, 746–751.

(37) Bisquert, J.; Fabregat-Santiago, F. In *Impedance Spectroscopy: A General Introduction and Application to Dye-Sensitized Solar Cells*; Kalyanasundaram, K., Ed.; CRC: Boca Raton, Florida, 2010; Chapter 12, pp 457–554.

(38) Bisquert, J.; Mora-Sero, I.; Fabregat-Santiago, F. Diffusion-Recombination Impedance Model for Solar Cells With Disorder and Nonlinear Recombination. *ChemElectroChem* **2014**, *1*, 289–296.

(39) Kulbak, M.; Cahen, D.; Hodes, G. How Important Is the Organic Part of Lead Halide Perovskite Photovoltaic Cells? Efficient $CsPbBr_3$ Cells. *J. Phys. Chem. Lett.* **2015**, *6*, 2452–2456.

(40) Nonnenmacher, M.; O'Boyle, M.; Wickramasinghe, H. Kelvin Probe Force Microscopy. *Appl. Phys. Lett.* **1991**, *58*, 2921–2923.

(41) Denk, W.; Pohl, D. W. Local Electrical Dissipation Imaged by Scanning Force Microscopy. *Appl. Phys. Lett.* **1991**, *59*, 2171–2173.

(42) Kuehn, S.; Loring, R. F.; Marohn, J. A. Dielectric Fluctuations and the Origins of Noncontact Friction. *Phys. Rev. Lett.* **2006**, *96*, 156103.

(43) Sze, S. M. *Physics of semiconductor devices*, 2nd ed.; Wiley-Interscience, 1981.

(44) Coffey, D. C.; Ginger, D. S. Time-Resolved Electrostatic Force Microscopy of Polymer Solar Cells. *Nat. Mater.* **2006**, *5*, 735–740.

(45) Giridharagopal, R.; Rayermann, G. E.; Shao, G.; Moore, D. T.; Reid, O. G.; Tillack, A. F.; Masiello, D. J.; Ginger, D. S. Submicrosecond Time Resolution Atomic Force Microscopy for Probing Nanoscale Dynamics. *Nano Lett.* **2012**, *12*, 893–898.

(46) Luria, J. L.; Hoepker, N.; Bruce, R.; Jacobs, A. R.; Groves, C.; Marohn, J. A. Spectroscopic Imaging of Photopotentials and Photoinduced Potential Fluctuations in a Bulk Heterojunction Solar Cell Film. *ACS Nano* **2012**, *6*, 9392–9401.

(47) Cox, P. A.; Glaz, M. S.; Harrison, J. S.; Peurifoy, S. R.; Coffey, D. C.; Ginger, D. S. Imaging Charge Transfer State Excitations in Polymer/Fullerene Solar Cells With Time-Resolved Electrostatic Force Microscopy. *J. Phys. Chem. Lett.* **2015**, *6*, 2852–2858.

(48) Karatay, D. U.; Harrison, J. S.; Glaz, M. S.; Giridharagopal, R.; Ginger, D. S. Fast time-resolved electrostatic force microscopy: Achieving sub-cycle time resolution. *Rev. Sci. Instrum.* **2016**, *87*, 053702.

(49) Chen, Y.; Yi, H. T.; Wu, X.; Haroldson, R.; Gartstein, Y. N.; Rodionov, Y. I.; Tikhonov, K. S.; Zakhidov, A.; Zhu, X. Y.; Podzorov, V. Extended carrier lifetimes and diffusion in hybrid perovskites revealed by Hall effect and photoconductivity measurements. *Nat. Commun.* **2016**, *7*, 12253.

(50) Labardi, M.; Lucchesi, M.; Prevosto, D.; Capaccioli, S. Broadband local dielectric spec-

troscopy. *Appl. Phys. Lett.* **2016**, *108*, 182906.

(51) Yazdanian, S. M.; Marohn, J. A.; Loring, R. F. Dielectric Fluctuations in Force Microscopy: Noncontact Friction and Frequency Jitter. *J. Chem. Phys.* **2008**, *128*, 224706.

(52) Hoepker, N.; Lekkala, S.; Loring, R. F.; Marohn, J. A. Dielectric Fluctuations over Polymer Films Detected Using an Atomic Force Microscope. *J. Phys. Chem. B* **2011**, *115*, 1449314500.

(53) Stipe, B. C.; Mamin, H. J.; Stowe, T. D.; Kenny, T. W.; Rugar, D. Noncontact Friction and Force Fluctuations between Closely Spaced Bodies. *Phys. Rev. Lett.* **2001**, *87*, 096801.

(54) Lekkala, S.; Hoepker, N.; Marohn, J. A.; Loring, R. F. Charge carrier dynamics and interactions in electric force microscopy. *J. Chem. Phys.* **2012**, *137*, 124701.

(55) Lekkala, S.; Marohn, J. A.; Loring, R. F. Electric Force Microscopy of Semiconductors: Cantilever Frequency Fluctuations and Noncontact Friction. *J. Chem. Phys.* **2013**, *139*, 184702.

(56) Crider, P. S.; Majewski, M. R.; Zhang, J.; Ouckris, H.; Israeloff, N. E. Local Dielectric Spectroscopy of Polymer Films. *Appl. Phys. Lett.* **2007**, *91*, 013102.

(57) Kronik, L.; Shapira, Y. Surface Photovoltage Phenomena: Theory, Experiment, and Applications. *Surf. Sci. Rep.* **1999**, *37*, 1–206.

(58) Calado, P.; Telford, A. M.; Bryant, D.; Li, X.; Nelson, J.; O'Regan, B. C.; Barnes, P. R. Evidence for Ion Migration in Hybrid Perovskite Solar Cells With Minimal Hysteresis. *Nat. Commun.* **2016**, *7*, 13831.

(59) Yin, W.-J.; Shi, T.; Yan, Y. Unusual Defect Physics in $CH_3NH_3PbI_3$ Perovskite Solar Cell Absorber. *Appl. Phys. Lett.* **2014**, *104*, 063903.

(60) Shi, T.; Yin, W.-J.; Hong, F.; Zhu, K.; Yan, Y. Unipolar Self-doping Behavior in Perovskite $CH_3NH_3PbBr_3$. *Appl. Phys. Lett.* **2015**, *106*, 103902.

(61) Moore, D. T. Crystal Growth of Organic-Inorganic Lead Halide Perovskites: Impact

of Kinetic Parameters on Morphology, Structure and Properties. Ph.D. thesis, Cornell University, Ithaca, New York, 2015.

Supporting Information: Coupled Slow and Fast Charge Dynamics in Cesium Lead Bromide Perovskite

Ali Moeed Tirmzi,[1] Ryan P. Dwyer,[1] Tobias Hanrath,[2] and John A. Marohn[1]

[1]*Department of Chemistry and Chemical Biology, Cornell University, Ithaca, New York 14853*

[2]*School of Chemical and Bimolecular Engineering, Cornell University, Ithaca, New York 14853*

S1. EXPERIMENTAL METHODS

A. Sample preparation

$CsPbBr_3$ was prepared on an indium tin oxide (ITO) substrate (Nanocs, $10\,\Omega$/sq.) following the procedure described in Ref. 1 in ambient conditions. ITO substrates were scrubbed with an Aquet liquid detergent/DI water solution, rinsed with DI water, and sonicated in a fresh Aquet solution for five minutes. The chips were rinsed, sonicated in pure DI water for five minutes, and dried with high pressure nitrogen gas. $10\,\mathrm{mL}$ of $1\,\mathrm{M}$ $PbBr_2$ (Alfa Aesar) in dimethylformamide was stirred in a closed vile at $75\,^\circ\mathrm{C}$ until all the $PbBr_2$ was dissolved. $15\,\mathrm{mg\,mL^{-1}}$ of CsBr (Chem Impex) was dissolved in methanol at $50\,^\circ\mathrm{C}$. $0.2\,\mu\mathrm{m}$ pore size PTFE filter was used to filter dissolved $PbBr_2$ and the solution was immediately used for spin coating. On a preheated ITO substrate, $PbBr_2$ solution was spin coated at 3000 rpm for 1 minute. The substrate was dried for 30 minutes at $75\,^\circ\mathrm{C}$, followed by dipping in CsBr solution at $50\,^\circ\mathrm{C}$. Films were rinsed with isopropyl alcohol and dried with high pressure nitrogen followed by annealing at $250\,^\circ\mathrm{C}$ for 10 minutes. The average film thickness was $\sim 500\,\mathrm{nm}$ (Figure S6).

B. Scanned probe microscopy

All experiments were performed under vacuum ($8 \times 10^{-7}\,\mathrm{mbar}$) in a custom-built scanning Kelvin probe microscope [2]. The cantilever was MikroMasch HQ:NSC18/Pt conductive probe. The resonance frequency and quality factor were obtained from ringdown measurement and found to be $\omega_c/2\pi = f_c = 66.545\,\mathrm{kHz}$ and $Q = 29\,900$ respectively. The manufacturer's specified resonance frequency and spring constant were $f_c = 60$ to $75\,\mathrm{kHz}$ and $k = 3.5\,\mathrm{N\,m^{-1}}$. The spring constant was determined by analysis of Brownian motion [3] and found to be between 4.8 and $10\,\mathrm{N\,m^{-1}}$. We attribute this variation to the poorly controlled position of the laser spot relative to the end of the cantilever. In our analysis, we used a spring constant of $k = 3.5\,\mathrm{N\,m^{-1}}$. Cantilever motion was detected using a fiber interferometer operating at $1490\,\mathrm{nm}$ (Corning SMF-28 fiber). The laser diode's (QPhotonics laser diode QFLD1490-1490-5S) DC current was set using a precision current source (ILX Lightwave LDX-3620) and the current was modulated at radiofrequencies using the input on the laser diode mount (ILX Lightwave LDM-4984, temperature controlled with ILX Lightwave LDT-5910B) [4]. The interferometer light was detected with a $200\,\mathrm{kHz}$ bandwidth photodetector (New Focus model 2011) and digitized at $1\,\mathrm{MHz}$ (National Instruments, PCI-6259). The cantilever was driven using a commercial phase locked loop (PLL) cantilever controller (RHK Technology, PLLPro2 Universal AFM controller), with typical PLL loop bandwidth $500\,\mathrm{Hz}$ (PLL feedback loop integral gain $I = 2.5\,\mathrm{Hz^{-1}}$, proportional gain $P = -5\,\mathrm{degrees/Hz}$). Frequency and amplitude were

determined by software demodulation of the cantilever response [5]. DC voltages were applied to the tip or sample with either a digital output from the PCI-6259 or a Keithley 2400 source measure unit.

Figure 2 experimental details. The measurements were performed with a constant excitation force F_{ex} using the PLLPro2. Because the excitation force was constant, the cantilever's steady-state amplitude A was related to cantilever's dissipation Γ: $F_{\mathrm{ex}} = A\Gamma\omega_{\mathrm{c}}$. The dissipation $\Gamma = \Gamma_{\mathrm{i}} + \Gamma_{\mathrm{s}}$ is the sum of an intrinsic dissipation Γ_{i} and a sample-induced dissipation Γ_{s}. The intrinsic dissipation $\Gamma_{\mathrm{i}} = k/(\omega_{\mathrm{c}}Q) = 280\,\mathrm{pN\,s\,m^{-1}}$ was determined from the measured ω_{c} and Q assuming $k = 3.5\,\mathrm{N\,m^{-1}}$. We fit the amplitude versus voltage data to extract γ_{s}:

$$A(V)(\Gamma_{\mathrm{i}} + \gamma_{\mathrm{s}}(V-\phi)^2)\omega_{\mathrm{c}} = A_0\Gamma_{\mathrm{i}}\omega_{\mathrm{c}} = F_{\mathrm{ex}}$$
$$A(V) = \frac{A_0\Gamma_{\mathrm{i}}}{\Gamma_{\mathrm{i}} + \gamma_{\mathrm{s}}(V-\phi)^2}, \tag{S1}$$

with fit parameters γ_{s}, ϕ and A_0 the cantilever's maximum amplitude. A wait time between points of $500\,\mathrm{ms}$ (greater than 3 times the $145\,\mathrm{ms}$ cantilever ringdown time) was used so that the measured amplitude was the steady-state amplitude.

The oscillator output of a PerkinElmer Signal Recovery 7265 DSP Lock-in amplifier was used as an AC source for the frequency shift versus modulation frequency experiments of Figure 4. In the variable temperature experiment, a temperature diode mounted near the cantilever was used to monitor the temperature [6]. Q_0 for each temperature was measured before illumination.

S2. SCANNED PROBE IMPEDANCE SPECTROSCOPY THEORY

The tip-sample electrostatic interaction is described by a potential energy

$$U = \frac{1}{2}\frac{q^2}{C(x)}. \tag{S2}$$

From Equation S2, we obtain the electrostatic force $F = -\partial U/\partial x$ (Equation 1). Substituting $Z = (R_{\mathrm{s}}^{-1} + j\omega C_{\mathrm{s}})^{-1}$ from the RC model of Figure 1 into Equation 3, we obtain a transfer function

$$\hat{H}(\omega) = \frac{1 + j\omega\tau_{\mathrm{fast}}}{1 + gj\omega\tau_{\mathrm{fast}}}. \tag{S3}$$

with magnitude, real and imaginary components

$$|\hat{H}(\omega)| = \left(\frac{1 + (\omega\tau_{\mathrm{fast}})^2}{1 + (g\omega\tau_{\mathrm{fast}})^2}\right)^{1/2} \tag{S4}$$

$$\mathrm{Re}\,\hat{H}(\omega) = H'(\omega) = \frac{1 + g(\omega\tau_{\mathrm{fast}})^2}{1 + (g\omega\tau_{\mathrm{fast}})^2} \tag{S5}$$

$$\mathrm{Im}\,\hat{H}(\omega) = H''(\omega) = \frac{(1-g)\omega\tau_{\mathrm{fast}}}{1 + (g\omega\tau_{\mathrm{fast}})^2}. \tag{S6}$$

The parameters τ_{fast} and g are given by Equation 4. Equations S4–S6 are plotted in Figure 1b.

A. Description of oscillating forces

All our experiments probe oscillating forces. We determine the relevant oscillating forces by controlling the displacement x and voltage $V(t) = V_{\text{ts}} - \phi$. In all cases, the displacement x is small, so we can linearize the force F to first order in x. The displacement x affects the force through the capacitance $C(x)$ and its derivatives, so a small displacement means one where $C_{\text{t}}' x / C_{\text{t}} \ll 1$ and $C_{\text{t}}'' x / C_{\text{t}}' \ll 1$. We linearize the capacitances about the point $x = 0$, replacing $C(x)$ and its derivatives with $C_{\text{t}} = C_{\text{tip}} = C(0)$. For the force of Equation 1 given by

$$F(x, q) = \frac{C'(x)}{2C(x)^2} q(x, V_{\text{ts}})^2,$$

the oscillating force is given by

$$\delta F = \left(\frac{\partial F}{\partial x}\right)_q x + \left(\frac{\partial F}{\partial q^2}\right)_x \delta q^2(x, V). \tag{S7}$$

The first term, representing the force gradient between the tip and sample at constant charge, is constant in all our experiments, but in practice is only relevant when the cantilever is oscillated at its resonance frequency ω_{c}. The two derivatives are

$$\left(\frac{\partial F}{\partial x}\right)_q = \frac{1}{2} \underbrace{\left(C_{\text{t}}'' - \frac{2C_{\text{t}}'^2}{C_{\text{t}}}\right)}_{C_q''} \frac{q^2}{C_{\text{t}}^2} = \frac{1}{2} C_q'' \frac{q^2}{C_{\text{t}}^2} \tag{S8}$$

$$\left(\frac{\partial F}{\partial q^2}\right)_x = \frac{C_{\text{t}}'}{2C_{\text{t}}^2}. \tag{S9}$$

In this formalism, it is useful to work with the variables

$$\Delta C'' = 2\frac{C_{\text{t}}'^2}{C_{\text{t}}} \quad \text{and} \quad C_q'' = C_{\text{t}}'' - \Delta C''. \tag{S10}$$

Using Equations S8–S10 to simplify Equation S7, the oscillating force is

$$\delta F = \frac{1}{2} C_q'' \frac{q^2}{C_{\text{t}}^2} x + \frac{C_{\text{t}}'}{2C_{\text{t}}^2} \delta q^2. \tag{S11}$$

For many experiments, δq is small, so $\delta q^2 \approx 2q\delta q$:

$$\delta F = \frac{1}{2} C_q'' \frac{q^2}{C_{\text{t}}^2} x + \frac{C_{\text{t}}'}{C_{\text{t}}^2} q \delta q. \tag{S12}$$

The experiments described in the text impose different oscillating charges, which to first order in x are

$$q(x, V) = \Big(\big(C_{\text{t}} + C_{\text{t}}' x\big)\, V(t)\Big) * H(t), \tag{S13}$$

where we abbreviate $V_{\rm ts} - \phi$ as $V(t)$. The idea behind this description of the oscillating charge is that *both* small tip displacements and small changes in applied tip-sample voltage change the electric field between the tip and sample, which causes charge to flow. For the experiment of Figure 1c, $V(t) = V_{\rm m} \cos \omega_{\rm m} t$ and $x \approx 0$ so the oscillating charge is

$$\delta q = C_{\rm t}(V_{\rm m} \cos \omega_{\rm m} t) * H(t) \tag{S14}$$

with a frequency domain magnitude $\delta\hat{q}(\omega_{\rm m}) = C_{\rm t} V_{\rm m} \hat{H}(\omega_{\rm m})$.

For the experiments of Figure 2, $V(t) = V - \phi$ and $x(t) = A \cos \omega_{\rm c} t$ so the oscillating charge is

$$\delta q = C_{\rm t}'(V - \phi)(A \cos \omega_{\rm c} t) * H(t). \tag{S15}$$

This is a small perturbation to the total charge so we can evaluate Eq. S15 in the frequency domain and plug the result into Eq. S12. The frequency domain magnitude is

$$\delta\hat{q}(\omega_{\rm c}) = C_{\rm t}' A (V - \phi)\, \hat{H}(\omega_{\rm c}). \tag{S16}$$

Using $q^2 = C_{\rm t}^2 (V_{\rm t} - \phi)^2$, we have

$$\delta\hat{F}(\omega_{\rm c})/A = \frac{1}{2} C_q''\, (V_{\rm t} - \phi)^2 + \frac{1}{2} \frac{2 C_{\rm t}'^2}{C_{\rm t}} \hat{H}(\omega_{\rm c})\, (V - \phi)^2. \tag{S17}$$

Using the definition of $\Delta C''$ in Equation S10, this simplifies to Equation 5.

B. Large modulation experiments

For the experiments of Figure 4, the total charge is

$$q = \Big(\left(C_{\rm t} + C_{\rm t}' x\right) \left(V_{\rm DC} + V_{\rm m} \cos \omega_{\rm m} t\right) \Big) * H(t) \tag{S18}$$

$$= C_{\rm t} V_{\rm DC} + C_{\rm t}' A V_{\rm DC} (\cos \omega_{\rm c} t) * H + C_{\rm t} V_{\rm m} (\cos \omega_{\rm m} t) * H + C_{\rm t}' A V_{\rm m} (\cos \omega_{\rm c} t \cos \omega_{\rm m} t) * H, \tag{S19}$$

where we have used $x = A \cos \omega_{\rm c} t$. This can be written compactly in the frequency domain, listing only terms with $\omega \geq 0$ since $\hat{q}(-\omega) = \hat{q}^*(\omega)$ because q is real:

$$\begin{aligned} \hat{q}(\omega > 0) = {} & C_{\rm t} V_{\rm DC}\, \delta(\omega) + C_{\rm t}' A V_{\rm DC} \hat{H}(\omega_{\rm c})\, \delta(\omega - \omega_{\rm c}) \\ & + C_{\rm t} V_{\rm m} \hat{H}(\omega_{\rm m})\, \delta(\omega - \omega_{\rm m}) \\ & + \frac{1}{2} C_{\rm t}' A V_{\rm m} \hat{H}(|\omega_{\rm c} - \omega_{\rm m}|)\, \delta(\omega - |\omega_{\rm c} - \omega_{\rm m}|) \\ & + \frac{1}{2} C_{\rm t}' A V_{\rm m} \hat{H}(\omega_{\rm c} + \omega_{\rm m})\, \delta(\omega - (\omega_{\rm c} + \omega_{\rm m})). \end{aligned} \tag{S20}$$

The Fourier transform of q^2 is $\hat{q} * \hat{q}$ by the convolution theorem. With $\widehat{q^2}$, we can write the oscillating force using the Fourier transform of Equation S11,

$$\delta\hat{F} = \frac{1}{2}\frac{C_q''}{C_\mathrm{t}^2}(\widehat{q^2} * x) + \frac{C_\mathrm{t}'}{2C_\mathrm{t}^2}\widehat{\delta q^2}. \tag{S21}$$

The convolutions $\hat{q} * \hat{q}$ and $\widehat{q^2} * \hat{x}$ result in *many* terms, but only a few important ones. First, since $\varepsilon = C_\mathrm{t}' A / C_\mathrm{t} \ll 1$, we keep only terms of order ε^1. Second, the DC frequency shift is only affected by the component of $\delta\hat{F}$ at ω_c; $\delta\hat{F}(\omega_\mathrm{c})$ depends on only two components of q^2:

$$\delta\hat{F}(\omega_\mathrm{c}) = \frac{1}{2}\frac{C_q''}{C_\mathrm{t}^2}A\widehat{q^2}(0) + \frac{C_\mathrm{t}'}{2C_\mathrm{t}^2}\widehat{\delta q^2}(\omega_\mathrm{c}). \tag{S22}$$

The $\omega = 0$ component affects the DC frequency shift through C_q'' and the $\omega = \omega_\mathrm{c}$ component affects the DC frequency shift through $\Delta C_\mathrm{t}''$, which can be extracted from $C_\mathrm{t}'/C_\mathrm{t}^2$ as above in Equation S17. Collecting the relevant terms, we have

$$\widehat{q^2}(0; V_\mathrm{DC}, V_\mathrm{m}) = C_\mathrm{t}^2 V_\mathrm{DC}^2 + \frac{1}{2}C_\mathrm{t}^2 V_\mathrm{m}^2 H(\omega_\mathrm{m})H(-\omega_\mathrm{m}) = C_\mathrm{t}^2 V_\mathrm{DC}^2 + \frac{1}{2}C_\mathrm{t}^2 V_\mathrm{m}^2 |H(\omega_\mathrm{m})|^2 \tag{S23}$$

$$\begin{aligned}\widehat{q^2}(\omega_\mathrm{c}; V_\mathrm{DC}, V_\mathrm{m}) = C_\mathrm{t} C_\mathrm{t}' A \Bigg(& V_\mathrm{DC}^2 H(0)H(\omega_\mathrm{c}) \\ & + \frac{1}{4}V_\mathrm{m}^2 \Big(H(\omega_\mathrm{c} - \omega_\mathrm{m})H(\omega_\mathrm{m}) + H(\omega_\mathrm{c} + \omega_\mathrm{m})H(-\omega_\mathrm{m}) \Big) \Bigg).\end{aligned} \tag{S24}$$

For the measurement, we take $\Delta f_\mathrm{DC}(V_\mathrm{m} = 2.83\,\mathrm{V}, V_\mathrm{DC} = -2.83\,\mathrm{V}) - \Delta f_\mathrm{DC}(V_\mathrm{m} = 0, V_\mathrm{DC} = -2.83\,\mathrm{V})$. This subtracts away the terms dependent only on V_DC, leaving only terms proportional to V_m^2. Plugging the V_m-dependent terms from Equations S23 and S24 into Equation S22 gives

$$\delta\hat{F}(\omega_\mathrm{c})/A = \underbrace{\frac{1}{4}C_q'' V_\mathrm{m}^2 |H(\omega_\mathrm{m})|^2}_{} + \frac{1}{8}\Delta C'' V_\mathrm{m}^2 \Big(H(\omega_\mathrm{c} + \omega_\mathrm{m})H(-\omega_\mathrm{m}) + H(\omega_\mathrm{c} - \omega_\mathrm{m})H(\omega_\mathrm{m}) \Big). \tag{S25}$$

Using Equation 7, the resulting cantilever frequency shift is

$$\begin{aligned}\Delta f_\mathrm{BLDS}(\omega_\mathrm{m}) = -\frac{f_\mathrm{c}}{4k}V_\mathrm{m}^2 \Bigg(& \frac{1}{2}C_q'' |H(\omega_\mathrm{m})|^2 \\ & + \frac{1}{4}\Delta C''\,\mathrm{Re}\Big(H(\omega_\mathrm{c} + \omega_\mathrm{m})H^*(\omega_\mathrm{m}) + H(|\omega_\mathrm{c} - \omega_\mathrm{m}|)H(\omega_\mathrm{m}) \Big) \Bigg).\end{aligned} \tag{S26}$$

All terms are proportional to the sample's response at the modulation frequency $\hat{H}(\omega_\mathrm{m})$. The normalized frequency shift plotted in Figure 4 is $\Delta f_\mathrm{BLDS}(\omega_\mathrm{m})/\Delta f_\mathrm{BLDS}(2\pi \times 0.1\,\mathrm{Hz})$.

S3. COMPARISON OF SAMPLE RESPONSE AT LOW-FREQUENCY AND ω_c

Figure 2 shows frequency-shift-parabola curvature increasing with light intensity. To distinguish a change in time constant τ_fast from an increase in photocapacitance, we performed voltage modulation

experiments at a frequency significantly below the cantilever resonance frequency. An increase in photocapacitance should increase the measured response *proportionally* at all frequencies, while a change in time constant should have only a small impact on the response at frequencies $\omega \ll \tau_{\text{fast}}^{-1}$. In Figure S2 we show that, apart from an initial 15 percent increase in low-frequency response when the sample was first exposed to light, only a 5 percent further increase was seen as the light intensity was increased. Therefore the large changes in curvature for the same light intensity cannot be explained by photocapacitance.

Modulated voltage force experiments

At a tip-sample distance of $h = 50\,\text{nm}$, a tip-sample voltage consisting of a variable DC offset and a small modulation was applied: $V_{\text{ts}} = V_{\text{DC}} + V_{\text{m}} \sin \omega_{\text{m}} t$. The DC voltage V_{DC} was applied to the sample's back electrode using a Keithley 2400 SMU. The modulation voltage $V_{\text{m}} = V_{\text{rms}}\sqrt{2} = 0.1\sqrt{2}$ V was applied at a frequency $\omega_{\text{m}}/2\pi = 523\,\text{Hz}$ using a Stanford Research Systems 830 DSP Lock-In Amplifier (SR830). The cantilever displacement signal at ω_{m} was measured using the SR830. The X and Y lock-in channels were digitized using the PCI-6259 and the average signal recorded. After the measurement, the slope m and intercept b for each channel were determined with a least square fit. The phase was determined using the slopes m_X, m_Y:

$$\theta = \arg(m_X + j\, m_Y) \tag{S27}$$

The quantity plotted in Figure S1 is the real component of the phased signal

$$Z' = \text{Re}\left((X + j\,Y)\, \exp(-j\theta)\right) \tag{S28}$$

divided by the rms-modulation voltage $V_{\text{rms}} = 0.1\,\text{V}$. This has units of $\text{nm}\,\text{V}^{-1}$. The corresponding rms-force on the cantilever is $F_{\text{rms}} = kZ'$ and should be proportional to $|\hat{H}(\omega_{\text{m}})|$ using the analysis of Equations S12 and S14 with $q = C_{\text{t}}(V_{\text{DC}} - \phi)$.

S4. TIP VOLTAGE EFFECT ON Q RECOVERY

By measuring time constant for Q recovery at different voltages, we show that tip voltage is not a major factor in determining the time constant (Table S1, Figure S3). The difference in the dissipation at different tip voltages corresponds to $\Gamma_s \propto (V - \phi)^2$.

S5. MULTIPLE TIME CONSTANTS

At a different location, we see evidence for multiple fast sample time constants crossing the cantilever frequency ω_c at different light intensities (Figure S4). As in Figure 2e, the dissipation has a peak ($I_{h\nu}^{\text{peak}} = 10\,\text{mW}\,\text{cm}^{-2}$). An increase in γ_s at $I_{h\nu} = 1000\,\text{mW}\,\text{cm}^{-2}$ is seen implying the existence of second dissipation peak at higher light intensities. The derivative of the curvature increases at light intensities near the dissipation peak, and flattens out again at higher light intensities. This behavior qualitatively matches the prediction of the simple one time constant model of Fig. 1b, Fig. 2(d,e) and Fig. 3. At the very highest light intensities, an increases in the derivative of curvature the accompanies the above noted increase in dissipation at $I_{h\nu} = 10 \times 10^3\,\text{mW}\,\text{cm}^{-2}$.

S6. NORMALIZED FREQUENCY SHIFT VERSUS MODULATION FREQUENCY

The solid lines shown in Figure 4 are plotted using

$$\Delta f(\omega_m) = \frac{C}{1 + (\omega_m \tau_{\text{fast}})^n} + d. \tag{S29}$$

The lines are only considered a guide to the eye. Comparing Figure 4 to Figure S5, we see that the sample's response as measured by the voltage modulation experiment depends on the sign of $V_{ts}(t) - \phi$.

S7. Q RECOVERY TIME CONSTANT

For the experiments of Figure 5, we converted the measured quality factor data $Q(t)$ into sample-induced dissipation Γ_s using the equation

$$\Gamma_s(t) = \frac{k}{\omega_c}\left(\frac{1}{Q(t)} - \frac{1}{Q_0}\right), \tag{S30}$$

where Q_0 is the quality factor far away from the surface without any applied tip voltage.

We used the following model to extract the time constant for Q recovery τ_Q in Figure 5. The modeled time-dependent sample dissipation $\Gamma_s^{\text{mod}}(t)$

$$\Gamma_s^{\text{mod}}(t) = \frac{2\Gamma_{\max}\,\omega_c \tau_{\text{fast}}(t)}{1 + \left(\omega_c \tau_{\text{fast}}(t)\right)^2} \tag{S31}$$

depends on the sample's time constant $\tau_{\text{fast}}(t)$. The time evolution of τ_{fast} was determined by the time-constant τ_Q according to the equations

$$k(t) = k_i + \left(k_f - k_i\right)\left(1 - e^{-(t-t_0)/\tau_Q}\right) \tag{S32}$$

$$\tau_{\text{fast}}(t) = k(t)^{-1}, \tag{S33}$$

with $t_0 = 133\,\mathrm{s}$ the time when the light was turned off, the initial rate $k_\mathrm{i} = \tau_\mathrm{fast}^{-1}(t_0)$, and the final rate $k_\mathrm{f} = \tau_\mathrm{fast}^{-1}(\infty)$. The fit parameters were k_i, k_f and τ_Q. Data acquired at $t > t_0$ was used for the fit. The maximum dissipation Γ_max was obtained from the measured data and was not included as a fit parameter.

The fit parameters from the data in Figure 5 are collected below.

Fit parameters for $I_{h\nu} = 1.3\,\mathrm{mW/cm^2}$ in Figure 5a (blue curve): $k_\mathrm{i} = (200 \pm 3)\,\mathrm{ms^{-1}}$, $k_\mathrm{f} = (34.0 \pm 0.3)\,\mathrm{ms^{-1}}$, and $\tau_Q = (8.5 \pm 0.2)\,\mathrm{s}$.

Fit parameters for $I_{h\nu} = 112\,\mathrm{mW/cm^2}$ in Figure 5a (red curve): $k_\mathrm{i} = (920 \pm 15)\,\mathrm{ms^{-1}}$, $k_\mathrm{f} = (49.0 \pm 0.5)\,\mathrm{ms^{-1}}$, and $\tau_Q = (12.4 \pm 0.1)\,\mathrm{s}$.

For Figure 5b, the time constants τ_Q calculated from the model described above: $\tau_Q(275K) = (30.9 \pm 0.7)\,\mathrm{s}$, $\tau_Q(293K) = (8.5 \pm 0.2)\,\mathrm{s}$, and $\tau_Q(313K) = (2.0 \pm 0.2)\,\mathrm{s}$.

S8. SURFACE POTENTIAL FIT

The surface potential in Figure 2c was fit to the equation

$$\phi = -c\,\log_{10}\left(1 + \frac{I}{I_0}\right), \tag{S34}$$

where $c = 72 \pm 4\,\mathrm{mV}$ and $I_0 = 0.17 \pm 0.06\,\mu\mathrm{W/cm^2}$.

S9. RISE TIME FOR DISSIPATION

The rise time for the dissipation when the light is switched ON is much faster than the corresponding τ_Q and is on the order of the ring-down time of the cantilever.(Figure S7).

REFERENCES

[1] Kulbak, M., Cahen, D. & Hodes, G. How important is the organic part of lead halide perovskite photovoltaic cells? Efficient $CsPbBr_3$ cells. *J. Phys. Chem. Lett.* **6**, 2452 – 2456 (2015). [url].

[2] Luria, J. L. *Spectroscopic Characterization of Charge Generation and Trapping in Third-Generation Solar Cell Materials Using Wavelength- and Time-Resolved Electric Force Microscopy*. Ph.D. thesis, Cornell University, Ithaca, New York (2011). [url].

[3] Hutter, J. L. & Bechhoefer, J. Calibration of atomic-force microscope tips. *Rev. Sci. Instrum.* **64**, 1868 – 1873 (1993). [url].

[4] Rugar, D., Mamin, H. & Guethner, P. Improved fiber-optic interferometer for atomic force microscopy. *Appl. Phys. Lett.* **55**, 2588 – 2590 (1989). [url].

[5] Yazdanian, S. M., Marohn, J. A. & Loring, R. F. Dielectric fluctuations in force microscopy: Noncontact friction and frequency jitter. *J. Chem. Phys.* **128**, 224706 (2008). [url].

[6] Smieska, L. M. *Microscopic Studies of the Fate of Charges in Organic Semiconductors: Scanning Kelvin Probe Measurements of Charge Trapping, Transport, and Electric Fields in p- and n-type Devices*. Ph.D. thesis, Cornell University, Ithaca, New York (2015). [url].

FIGURES

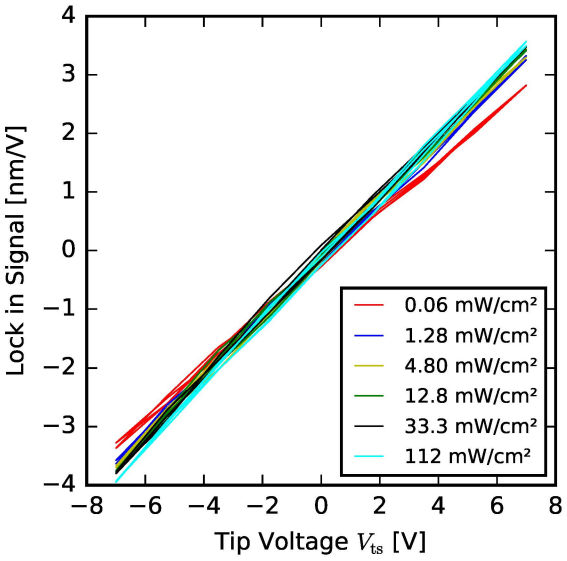

FIG. S1. Sample response at $\omega_m/2\pi = 523\,\mathrm{Hz}$. Signal proportional to $(V_{DC} - \phi)|\hat{H}(\omega_m)|/k$. Experimental parameters: $h = 50\,\mathrm{nm}$, $V_m = V_{rms}\sqrt{2} = 0.1\sqrt{2}\ \mathrm{V}$.

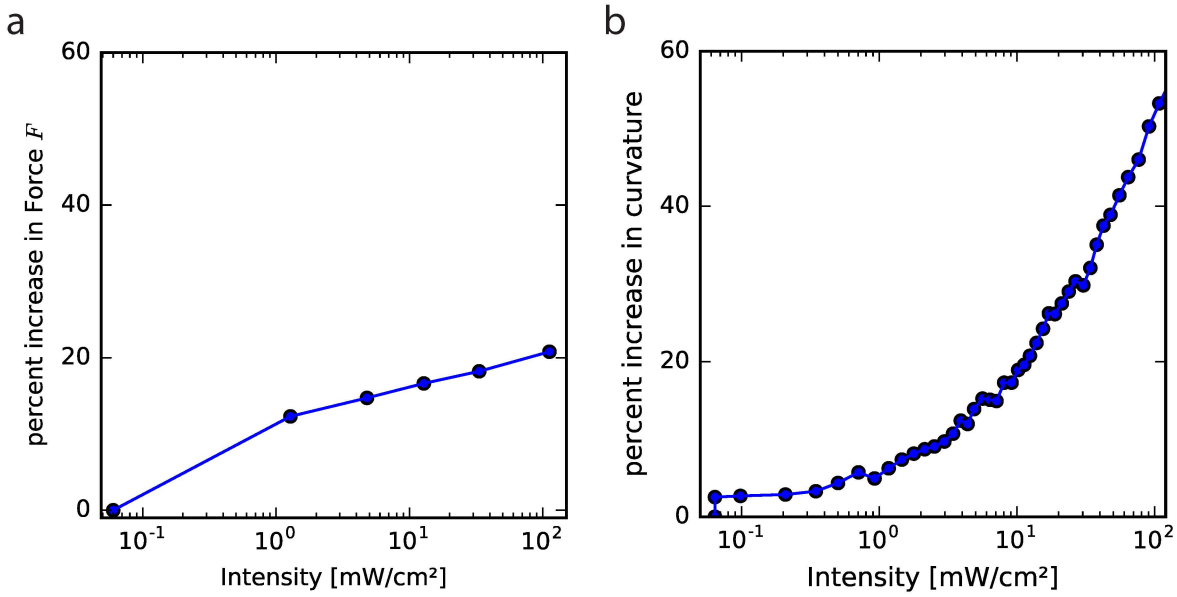

FIG. S2. Comparison of sample response measured at $\omega_{\rm m}/2\pi = 523\,{\rm Hz}$ and $\omega_{\rm c}/2\pi = 66.545\,{\rm kHz}$. (a) Sample response measured via the modulated voltage data of Fig. S1. Experimental parameters: $h = 50\,{\rm nm}$, $V_{\rm m} = V_{\rm rms}\sqrt{2} = 0.1\sqrt{2}$ V. (b) Sample response measured at the resonance frequency via the cantilever frequency shift and amplitude data of Figure 2.

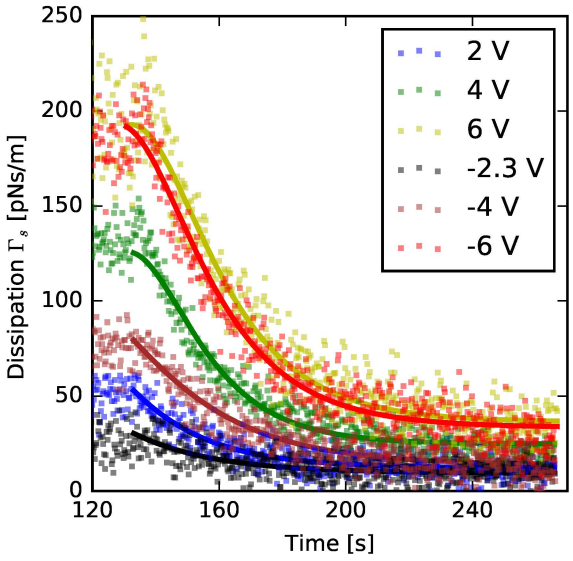

FIG. S3. Dissipation at different tip voltages. The tip voltage does not change the Q-recovery time constant significantly. Time constants collected in Table S1. Experimental parameters: light intensity $I_{h\nu} = 4.8\,\mathrm{mW\,cm^{-2}}$, $T = 275\,\mathrm{K}$, and $h = 200\,\mathrm{nm}$.

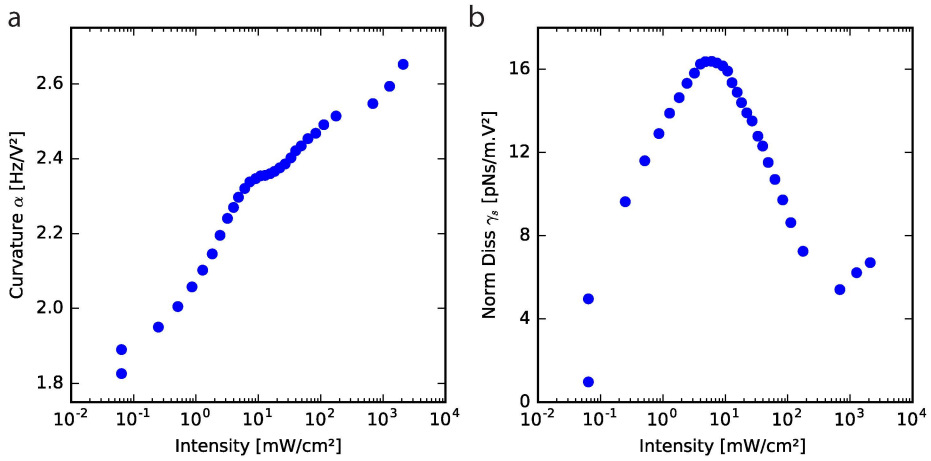

FIG. S4. (a) Curvature versus light intensity. (b) Normalized dissipation versus light intensity. Experimental parameters: $h = 200\,\mathrm{nm}$, frequency shift and amplitude parabolas acquired with $N = 28$ points from $V_{\mathrm{ts}} = -4\,\mathrm{V}$ to $4\,\mathrm{V}$.

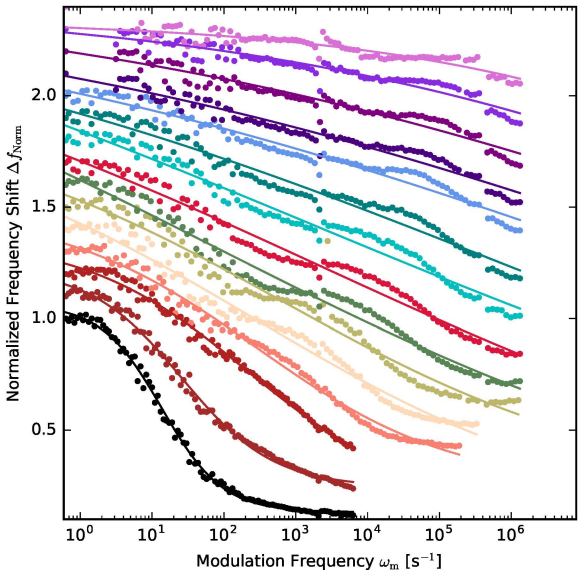

FIG. S5. Normalized frequency shift vs. modulation frequency for increasing light intensities (offset by 0.1) for negative sample charge. We applied a tip-sample voltage $V_{\mathrm{ts}} = \phi + V_{\mathrm{m}} + V_{\mathrm{m}} \cos(\omega_{\mathrm{m}} t)$ so that the sample charge was always negative ($V_{\mathrm{ts}}(t)$ always more than ϕ). At each light intensity, the surface potential ϕ was measured before performing the modulation experiment. $I_{h\nu}$ from bottom to top: 0, 0.064, 0.512, 1.28, 3.2, 4.8, 12.8, 22, 33, 49, 83, 112,176, 685, 2095 $\mathrm{mW/cm^2}$.

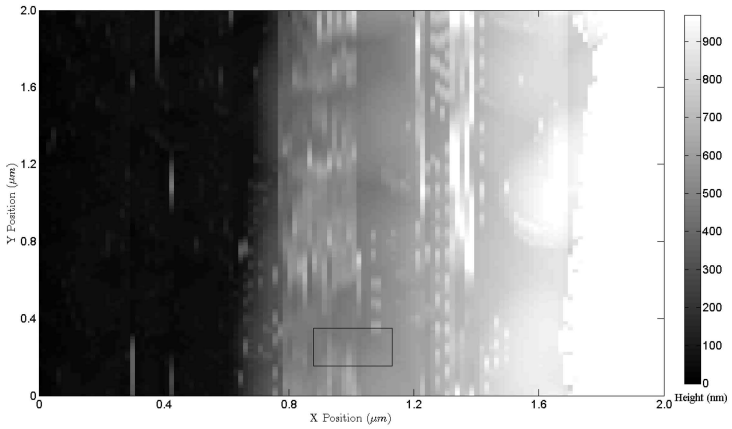

FIG. S6. Representative AFM image of the film. Dark area corresponds to places with no film coverage. The area in the box corresponds to the location where the experiments of Figure 5 were performed.

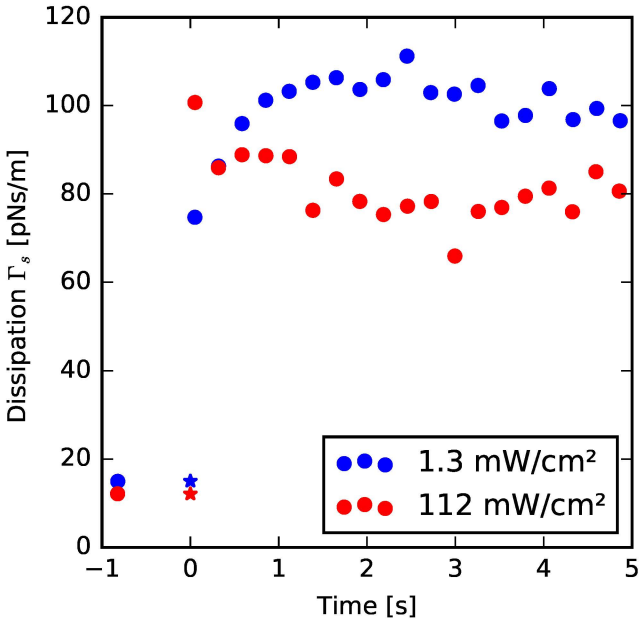

FIG. S7. Rise time for the dissipation data shown in Figure 5a. $V_{\rm ts} = -4\,{\rm V}$ is applied $60\,{\rm sec}$ before the start of measurement. Dark value for dissipation is measured before the light is switched ON at $t = 0$. The points at $t = 0$ have been added for clarity. The rise time for the dissipation is much faster than the corresponding τ_Q and is on the order of the ring-down time for the cantilever.

TABLES

Tip Voltage V_{ts} [V]	Time constant τ_Q [s]
2	21.3
4	17.6
6	20.7
-2.3	24.6
-4	26.5
-6	20.9

TABLE S1. Dependence of Q-recovery time constant on tip voltage at the same light intensity and temperature. Time constants calculated from the data of Figure S3 using the model of Section S7.